2016

Earliest hominin occupation of Sulawesi, Indonesia

Gerrit D. van den Bergh
University of Wollongong, gert@uow.edu.au

Bo Li
University of Wollongong, bli@uow.edu.au

Adam R. Brumm
University of Wollongong, abrumm@uow.edu.au

Rainer Grün
Griffith University, rainer.grun@anu.edu.au

Dida Yurnaldi
University of Wollongong, dy657@uowmail.edu.au

See next page for additional authors

Publication Details

van den Bergh, G. D., Li, B., Brumm, A., Gruen, R., Yurnaldi, D., Moore, M. W., Kurniawan, I., Setiawan, R., Aziz, F., Roberts, R. G., Suyono, , Storey, M., Setiabudi, E. & Morwood, M. J. (2016). Earliest hominin occupation of Sulawesi, Indonesia. Nature, 529 (7585), 208-211.

Earliest hominin occupation of Sulawesi, Indonesia

Abstract

Sulawesi is the largest and oldest island within Wallacea, a vast zone of oceanic islands separating continental Asia from the Pleistocene landmass of Australia and Papua (Sahul). By one million years ago an unknown hominin lineage had colonized Flores immediately to the south1, and by about 50 thousand years ago, modern humans (Homo sapiens) had crossed to Sahul2, 3. On the basis of position, oceanic currents and biogeographical context, Sulawesi probably played a pivotal part in these dispersals4. Uranium-series dating of speleothem deposits associated with rock art in the limestone karst region of Maros in southwest Sulawesi has revealed that humans were living on the island at least 40 thousand years ago (ref. 5). Here we report new excavations at Talepu in the Walanae Basin northeast of Maros, where in situ stone artefacts associated with fossil remains of megafauna (Bubalus sp., Stegodon and Celebochoerus) have been recovered from stratified deposits that accumulated from before 200 thousand years ago until about 100 thousand years ago. Our findings suggest that Sulawesi, like Flores, was host to a long-established population of archaic hominins, the ancestral origins and taxonomic status of which remain elusive.

Disciplines

Medicine and Health Sciences | Social and Behavioral Sciences

Publication Details

van den Bergh, G. D., Li, B., Brumm, A., Gruen, R., Yurnaldi, D., Moore, M. W., Kurniawan, I., Setiawan, R., Aziz, F., Roberts, R. G., Suyono, , Storey, M., Setiabudi, E. & Morwood, M. J. (2016). Earliest hominin occupation of Sulawesi, Indonesia. Nature, 529 (7585), 208-211.

Authors

Gerrit D. van den Bergh, Bo Li, Adam R. Brumm, Rainer Grün, Dida Yurnaldi, Mark W. Moore, Iwan Kurniawan, Ruly Setiawan, Fachroel Aziz, Richard G. Roberts, - Suyono, Michael Storey, Erick Setiabudi, and Michael J. Morwood

Title: Earliest hominin occupation of Sulawesi, Indonesia.

Authors: Gerrit D. van den Bergh[1,2†], Bo Li[1], Adam Brumm[3,4], Rainer Grün[5], Dida Yurnaldi[1,6], Mark W. Moore[7], Iwan Kurniawan[6], Ruly Setiawan[6], Fachroel Aziz[6], Richard G. Roberts[1], Suyono[6], Michael Storey[8], Erick Setiabudi[6], Michael J. Morwood[1#]

Author affiliations:

[1]Centre for Archaeological Science, School of Earth & Environmental Sciences, University of Wollongong, Wollongong, NSW 2522, Australia.

[†]E-mail: gert@uow.edu.au

[2] Naturalis Biodiversity Center, 2333 CR Leiden, The Netherlands.

[3]Environmental Futures Research Institute, Griffith University, Nathan, QLD 4111, Australia

[4]School of Earth & Environmental Sciences, University of Wollongong, Wollongong, NSW 2522, Australia.

[5]Research School of Earth Sciences, The Australian National University, Canberra, ACT 0200, Australia.

[6]Geology Museum Bandung, Geological Agency, Jl. Diponegoro 57, Bandung 40122, Indonesia.

[7]Archaeology, School of Humanities, University of New England, Armidale, NSW 2350, Australia.

[8]Department of Environmental, Social and Spatial Change, Roskilde University, DK-4000 Roskilde, Denmark.

[#]Deceased

Sulawesi is the largest and oldest island in Wallacea, the vast zone of oceanic islands separating continental Asia from the Pleistocene landmass of Australia and Papua (Sahul) (Fig. 1). By one million years (myr) ago an unknown hominin lineage had colonised Flores immediately to the south[1], and, by around 50 thousand years (kyr) ago, modern humans (*Homo sapiens*) had crossed to Sahul[2,3]. On the basis of position, oceanic currents and biogeographical context, Sulawesi is likely to have played a pivotal role in these dispersals[4]. Until now, however, the oldest archaeological evidence for humans on the island was around 40 kyr in age, from direct Uranium-series dating of speleothem deposits associated with rock art from the limestone karst region of Maros in the south-western peninsula[5]. It is now emerging that hominins may have been present in the Maros karst prior to the expansion of modern humans into Southeast Asia[6]. Here we report our recent excavations at Talepu in the Walanae Basin northeast of Maros, which have yielded *in situ* stone artefacts in association with fossil remains of megafauna (*Bubalus* sp., *Stegodon* and *Celebochoerus*) in stratified deposits spanning the period between around 200 kyr to 100 kyr ago, and likely much earlier. Our findings suggest that Sulawesi, like Flores, was host to a long-established population of archaic hominins, the ancestral origins of which remain elusive.

In the late-1940s the discovery of 'Palaeolithic' stone artefacts in association with Pleistocene fossil fauna in the Walanae Basin of South Sulawesi[7] led to considerable speculation as to the time depth of human occupation on this island[8,9]. The lithic assemblages comprised cores, choppers and flakes (the so-called 'Cabenge Industry'), all of which derived from undated surface collections made along the eastern side of the Walanae River[7-9] – the course of which follows an elongated north-south trending fault-bounded basin, the Walanae Depression (WD) (**Fig. 1**). Fossils of several now-extinct species, including two pygmy proboscideans, giant tortoise and a large endemic suid, *Celebochoerus*, were recovered from the same unstratified contexts[10,11], but also from *in situ* excavations at various sites[12]. Despite protracted investigations, the stratigraphic context and time range of the Cabenge industry remained unresolved due to the lack of *in situ* stone artefacts[12].

To clarify these issues, we conducted surveys in the Cabenge area between 2007 and 2012, leading to the discovery of four new sites with stone artefacts *in situ* in stratigraphic context. At Talepu, one of the four newly-discovered sites, we undertook deep-trench excavations. The site is located 3 km southeast of Cabenge and 13 km downstream from the point where the Walanae River leaves its confining valley and enters a widening, actively subsiding floodplain towards the north (**Fig. 1, see also Extended Data Fig. 1**). During the Pleistocene, east-west compression and wrench faulting along the Walanae Fault zone resulted in the uplift of the Sengkang Anticline and the southern part of the WD[13,14] .In these uplifted areas the folded Pliocene-Pleistocene sedimentary sequences of the Walanae Formation are now exposed[12]. In the northern part of the WD, compressional down-folding facilitated the continuing accumulation of fluvio-lacustrine sediments during the Pleistocene up to recent times. The site of Talepu (4°22'06.5"S, 119°59'01.7"E) is located near the hinge line between the uplifted southern and the subsiding northern part of the WD.

Our excavations focused on the northernmost hill of an elongated ridge near Talepu village, some 600 m west of the Walanae River (**Fig.1c**). The summit of Talepu Hill lies 32 m above sea level and 18 m above the adjacent Walanae River floodplain. The deposits exposed along this ridge comprise a coarsening-upward sequence of sub-horizontal fluvio-estuarine sand and silt layers overlaid by alluvial cobble gravels (**Fig. 1c, Extended Data Fig. 2**). Two deep excavations were undertaken at Talepu (Trenches T2 and T4) to provide a combined 18.7 m-long stratigraphic section in which five main sedimentary units are exposed. In descending order of depth, these are: Units A, B, C, D and E (**Fig. 2**).

These excavations have revealed the first evidence of *in situ* stone artefacts in securely stratified and dated contexts within the Walanae Basin. For instance, the T2 excavation yielded a total of 318 stone artefacts between the surface and 4.9 m depth (**Fig. 3a-i; Extended Data Fig. 3b**). The artefacts are associated with high-energy fluvial gravel deposits of Unit A. Hence, the majority of the artefacts (81%) are water-rolled to various degrees. The main source of raw material was coarse- to medium-grained silicified limestone, with minor use made of fine-grained chert. Most artefacts consist of medium- to large-sized flakes and debitage, with cores comprising 22.3% of the assemblage. The flakes were struck by hard-hammer percussion without prior platform preparation, from water-rolled cobbles found in the conglomerates of Unit A. Cobbles were reduced unifacially and bifacially.

In T4 we recovered 41 stone artefacts from the topsoil and colluvium down to a depth of 90 cm. However, three *in situ* silicified limestone artefacts were found in older strata exposed in T4 (**Fig. 3j-m**), all within the basal clayey silt of Unit E_2. These artefacts now provide the stratigraphically earliest evidence for human activity at Talepu. They comprise unmodified flakes from 2.2-2.4 m depth (N = 2) and 3.0-3.1 m depth (N = 2), and shatter fragments (N =

3) probably created in percussion flaking. These artefacts bear no evidence of water transport; indeed, Unit E did not yield any clasts indicative of high-energy water flow. The two flakes from 3 m depth are made of the same distinctive mottled silicified limestone and appear to have been removed from the same core (**Fig. 3j-k**).

Only one identifiable fossil was found in T2, a bovid molar fragment from 4 m depth (**Fig. 3t**). The bovid molar fragment falls just above the size range of *Bubalus depressicornis*, the extant lowland anoa (**Extended Data Fig. 10**). In T4, eight *Celebochoerus* dental elements, including a lower canine (**Fig. 3o**) and three unidentifiable bone fragments were excavated from the clayey silt interval of Unit E_2 between 3.1 and 4 m depth below the surface, and just beneath the lowest stone artefacts. At least some of these fossil remains can be ascribed to a single individual (**Fig. 3q**). A *Stegodon* milk molar fragment was also recovered at 1.9 to 2 m depth (**Fig. 3r**) and a dermal scute of a crocodile from 3.9 to 4 m depth.

Palaeomagnetic samples from silty clay layers of Units A, C and E indicate normal magnetic polarities for all sampled levels (**Extended Data Figs. 3e, 4**). To determine the age of the Talepu deposits we obtained Uranium-series ages of excavated teeth and bones from Unit E, using laser ablation ICP-MS[15,16] (see **Methods: U-series dating**). Sequential laser spot analyses were undertaken on cross sections of eight *Celebochoerus* fossils found up to one metre below the deepest stone artefacts in the same silty clay unit. The data sets were combined for each sample and a single age estimate was calculated using the diffusion-absorption-decay model[17]. Most of the age results had infinite positive error bounds and so it was only possible to calculate minimum ages[18]. The U-series results (**Supplementary Table 1**) consistently indicate that the fossil samples are older than ~350 kyr. The deepest stone artefacts recovered from the same fine-grained Unit E_2 are slightly younger than this minimum U-series age.

To further constrain the age of the artefacts, a multiple-elevated-temperature post-infrared infrared stimulated luminescence (post-IR IRSL or MET-pIRIR) procedure on potassium-rich feldspar was undertaken on five samples spanning the entire sequence. Four analysed samples from T2 yielded ages in accordance with their stratigraphic order: 103 ± 9 kyr at 3 m depth to 156 ± 19 kyr at 10 m depth (see **Fig. 2**, **Supplementary Info: Optical Dating** and **Supplementary Table 2**). The results suggest that the upper age limit of the cultural sequence at Talepu is around ~100 kyr. The 156 ± 19 kyr age calculation derives from feldspar samples collected near the top of Unit D, which overlies the sedimentary layer (Unit E) from which the deepest artefacts were excavated >3 m below. The oldest securely dated evidence for stone artefacts at Talepu, therefore, dates to 118-194 kyr ago (95% confidence interval [2-σ]), although human occupation of the site clearly occurred at greater stratigraphic depths. Lastly, a sample taken at a depth of 8 m in the lower trench (T4) yielded a minimum age of ~190 kyr. This older age estimate is stratigraphically correct and corroborates the minimum U-Series ages of ~350 kyr for the fossil remains from Unit E. The maximum age for the deepest fossil fauna from T4 cannot be established at present; however, assuming the normal magnetic polarities are all within the Brunhes Chron, it should fall between 350 and 780 kyr ago.

Based on the results of our Talepu excavations it is now possible to conclude that the initial peopling of Sulawesi took place at least 118 kyr ago. The identity of these early inhabitants is of considerable interest given prior assumptions that Sulawesi was only ever colonised by *H. sapiens*, who are currently thought to have arrived in the region around 50 kyr ago[19-22]. The earliest *H. sapiens* skeletal remains from Southeast Asia are about 45 kyr old[23,24] ; however, modern human fossils dating to ~120 kyr ago occur in the Levant[25], and possibly in Southeast Asia[26] at a similar time. It is not inconceivable, therefore, that *H. sapiens* dispersed from Africa soon after their evolution there, spread to the easternmost tip of continental Asia (Sunda), and then crossed to Wallacea between ~200 to 120 kyr ago. While this is one possibility, as we have already noted early hominins had reached Flores by one million years ago[1], perhaps by accidental drifting on tsunami debris[4]. It is plausible to suggest, therefore, that they could have been conveyed in this manner to the far larger and less remote island of Sulawesi at an equivalent, earlier, or later time.

For now, the absence of Pleistocene human fossils on Sulawesi precludes definitive answers. On the basis of the known distribution of hominins in the region, however, which includes *H. floresiensis* and a source of potential island colonisers, *Homo erectus*, on the southern margin of Sunda (present-day Java) from 1.5 myr ago until ~140 kyr ago[27,28] , as well as, perhaps, Denisovans, whose range could well have extended into Wallacea[29], our Talepu findings provide compelling evidence that early hominins were established on Sulawesi by the late Middle Pleistocene period. If such was the case, then the most likely points of origin for these colonisers are Borneo to the west and the Philippines to the north[30], the former a part of mainland Asia and the latter the northern extremity of Wallacea, suggesting at least some islands in the wider region harbor undiscovered records of archaic hominins.

References

1. Brumm, A. *et al.* Hominins on Flores, Indonesia, by one million years ago. *Nature* **464**, 748-752 (2010).
2. Roberts, R. *et al.* Single-aliquot and single-grain optical dating confirm thermoluminescence age estimates at Malakunanja II rock shelter in northern Australia. *Ancient TL* **16**, 19-24 (1998).
3. O Connor, S. New evidence from East Timor contributes to our understanding of earliest modern human colonisation east of the Sunda Shelf. *Antiquity* **81**, 523-535 (2007).
4. Morwood, M. & Van Oosterzee, P. *The Discovery of the Hobbit: The Scientific Breakthrough that Changed the Face of Human History.*, (Random House Australia, 2006).
5. Aubert, M. *et al.* Pleistocene cave art from Sulawesi, Indonesia. *Nature* **514**, 223-227 (2014).
6. Brumm, A. *et al. Late Pleistocene hominins in the Maros karst of Sulawesi, Indonesia* (submitted).
7. van Heekeren, H. R. Early man and fossil vertebrates on the island of Celebes. *Nature* **163**, 492 (1949).
8. Bartstra, G.-J., Keates, S. G., Basoeki & Kallupa, B. On the dispersion of Homo Sapiens in eastern Indonesia: The Palaeolithic of south Sulawesi. *Current Anthropology* **32**, 317-321 (1991).
9. van Heekeren, H. R. *The Stone Age of Indonesia*. (Martinus Nijhoff, 1972).

10 Hooijer, D. A. Pleistocene Vertebrates from Celebes: Celebochoerus Heekereni Nov. Gen. Nov. Spec. *Proceedings of the Koninklijke Nederlandse Akademie van Wetenschappen* **51**, 1024-1032 (1948).

11 Hooijer, D. A. Quaternary mammals west and east of Wallace's Line. *Netherlands Journal of Zoology* **25**, 46-56 (1974).

12 van den Bergh, G. D. The Late Neogene elephantoid-bearing faunas of Indonesia and their palaeozoogeographic implications: a study of the terrestrial faunal succession of Sulawesi, Flores and Java, including evidence for early hominid dispersal east of Wallace's Line. *Scripta Geologica* **117**, 1-419 (1999).

13 Grainge, A. M. & Davies, K. G. in *Proceedings of the Annual Convention of the Indonesian Petroleum Association.*12th edn 207-227 (Indonesian Petroleum Association).

14 Sukamto, R. in *Geological Map of Indonesia, Sheet VIII: Ujung Pandang.* (Geological Research and Development Centre, Bandung, 1975).

15 Eggins, S., Grün, R., Pike, A. W. G., Shelley, M. & Taylor, L. ^{238}U, ^{232}Th profiling and U-series isotope analysis of fossil teeth by laser ablation-ICPMS. *Quaternary Science Reviews* **22**, 1373-1382 (2003).

16 Eggins, S. M. *et al.* In situ U-series dating by laser-ablation multi-collector ICPMS: new prospects for Quaternary geochronology. *Quaternary Science Reviews* **24**, 2523-2538 (2005).

17 Sambridge, M., Grün, R. & Eggins, S. U-series dating of bone in an open system: the diffusion-adsorption-decay model. *Quaternary Geochronology* **9**, 42-53 (2012).

18 Grün, R., Aubert, M., Hellstrom, J. & Duval, M. The challenge of direct dating old human fossils. *Quaternary International* **223**, 87-93 (2010).

19 Keates, S. G. Notes on the Palaeolithic finds from the Walanae valley, southwest Sulawesi, in the context of the late Pleistocene of island Southeast Asia. *Modern Quaternary Research in Southeast Asia* **18**, 95-110 (2004).

20 Summerhayes, G. R. *et al.* Human adaptation and plant use in highland New Guinea 49,000 to 44,000 years ago. *Science* **330**, 78-81 (2010).

21 O'Connor, S., Ono, R. & Clarkson, C. Pelagic fishing at 42,000 years before the present and the maritime skills of modern humans. *Science* **334**, 1117-1121 (2011).

22 Mellars, P. Why did modern human populations disperse from Africa ca. 60,000 years ago? A new model. *Proceedings of the National Academy of Sciences* **103**, 9381-9386 (2006).

23 Barker, G. *et al.* The 'human revolution'in lowland tropical Southeast Asia: the antiquity and behavior of anatomically modern humans at Niah Cave (Sarawak, Borneo). *Journal of Human Evolution* **52**, 243-261 (2007).

24 Storm, P. *et al.* U-series and radiocarbon analyses of human and faunal remains from Wajak, Indonesia. *Journal of Human Evolution* **64**, 356-365 (2013).

25 Grün, R. *et al.* U-series and ESR analyses of bones and teeth relating to the human burials from Skhul. *Journal of Human Evolution* **49**, 316-334 (2005).

26 Westaway, K. E. *et al.* Age and biostratigraphic significance of the Punung Rainforest Fauna, East Java, Indonesia, and implications for Pongo and Homo. *Journal of Human Evolution* **53**, 709-717 (2007).

27 Zaim, Y. *et al.* New 1.5 million-year-old *Homo erectus* maxilla from Sangiran (central Java, Indonesia). *Journal of Human Evolution* **61**, 363-376 (2011).

28 Indriati, E. *et al.* The age of the 20 meter Solo River terrace, Java, Indonesia and the survival of *Homo erectus* in Asia. *PloS one* **6**, e21562 (2011).

29 Cooper, A. & Stringer, C. Did the Denisovans Cross Wallace's Line? *Science* **342**, 321-323 (2013).

30 Mijares, A. S. *et al.* New evidence for a 67,000-year-old human presence at Callao Cave, Luzon, Philippines. *Journal of Human Evolution* **59**, 123-132 (2010).

Supplementary Information is linked to the online version of the paper at www.nature.com/nature.

ACKNOWLEDGMENTS

This research was supported by grants from the Australian Research Council (ARC) to M.J.M. (DP0770234/ DP1093342), G.D.v.d.B. (FT100100384), and funds from the Geological Survey Institute of Indonesia. L.B. and R.G.R. were supported by ARC Fellowships FT140100384 and FL130100116. A.B.'s involvement was supported by ARC fellowship DE130101560. The stone tool analysis was supported by ARC Fellowship DP1093342 to M.W.M. The fieldwork was authorized by the directors of the Geological Survey Institute of Indonesia, A. Djumarma Wirakusumah and Y. Kusumahbrata. We further acknowledge the Indonesian State Ministry of Research and Technology and the National Centre for Archaeology in Jakarta (ARKENAS), for facilitating the research. Field assistants included H. Oktaviana, Dadang, S. Sudjarwadi, Ngaliman, T. Suryana and U.P. Wibowo. During the excavations we were assisted by the landowner, Wahe, and 11 other local labourers. Leslie Kinsley assisted with the U-series analysis. We thank Kira Westaway, Darryl Granger, Brad Pillans and Brian Jones for additional field support. Susan Hayes is thanked for providing feedback on the manuscript.

AUTHOR CONTRIBUTIONS

M.J.M. and G.D.v.d.B. conceived the study with F.A., as part of a wider project led by M.J.M., in collaboration with A.B., I.K., S. and E.S. Samples for optical dating were collected and analysed by B.L. and R.G.R.. R.G. conducted the U-series dating. A.B. and M.W.M. identified and analysed the stone artefacts. G.D.v.d.B and I.K. analysed the fossil specimens. G.D.v.d.B. and R.S. recorded the site stratigraphy. D.Y. collected and analysed samples for palaeomagnetism. M.S. analysed samples for $^{39}Ar/^{40}Ar$ dating. S. conducted a regional geological survey supervised by G.D.v.d.B. and M.J.M. G.D.v.d.B and A.B. wrote the manuscript.

AUTHOR INFORMATION

Reprints and permissions information is available at www.nature.com/reprints.

The authors declare they have no competing financial interests.

Correspondence and requests for material should be addressed to G.D.v.d.B (gert@uow.edu.au).

MAIN TEXT FIGURES

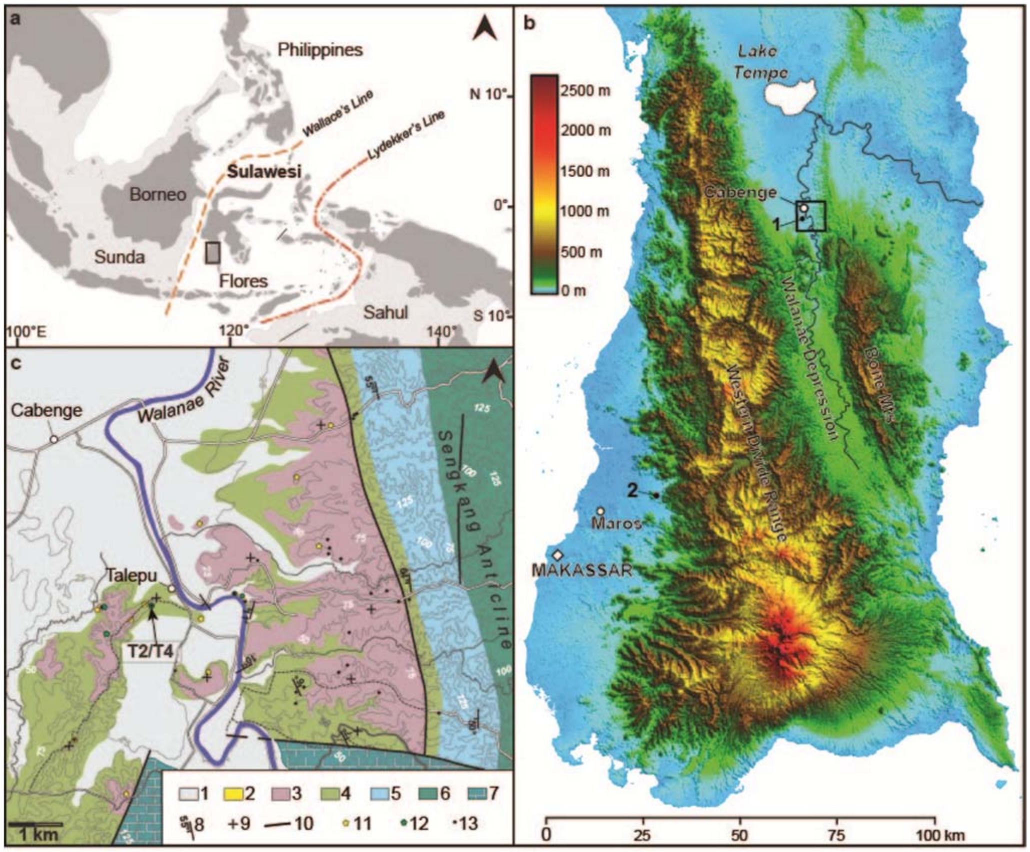

Fig 1. Study area location and geological setting. **a**, Map of Southeast Asia showing the continental regions of Sunda and Sahul and the oceanic island zone (Wallacea) that separates them. Wallacea lies between two major biogeographical boundaries (represented by broken lines): Wallace's Line to the west, and Lydekker's Line to the east. Sulawesi is the largest island in Wallacea. The lightly shaded area depicts continental shelf regions exposed during periods of low sea level (-120 m). Panel **b** shows the area enclosed by the rectangle; **b**, Digital Elevation Map of the south-western peninsula of Sulawesi. The numbered black dots represent sites mentioned in the text: **1**, Talepu (near the town Cabenge); **2**, Leang Bulu Bettue (near the town of Maros). Talepu is situated near the boundary between the uplifted southern part of the Walanae Depression and the actively subsiding northern part. Panel **c**

shows the area enclosed by the black rectangle; **c**, Geological map of the Talepu area in the Walanae Depression. The area where most artefacts and fossils originate from is characterized by sub-horizontal layering, fault-bounded to the east by the steeply west dipping strata of the western flank of the Sengkang Anticline, which is a deformational structure formed in response to east-west compression and strike-slip movements along the Walanae Fault zone. Movements along this fault zone influenced deposition in the Walanae Depression during the Pleistocene. Geological and archaeological features depicted: 1, Modern alluvium; 2, Late Pleistocene alluvial terrace deposits (only developed along the east bank of the Walanae River 2 km east of Talepu); 3, Fluvio-lacustrine facies pertaining to the upper part of the Beru Member of the Walanae Formation; 4, Fluvio-estuarine facies of the lower part of the Beru Member, characterized by tidally influenced sediments; 5, Shallow marine facies of the Samaoling Member (Walanae Formation); 6, Deep marine marl facies of the Burecing Member (Walanae Formation); 7, Coral reef facies of the Walanae Formation; 8, Strike and dip; 9, Sub-horizontal layering; 10, Major fault; 11, Surface-collected stone artefacts; 12, Sites with *in situ* stone artefacts; 13, Fossil vertebrate localities.

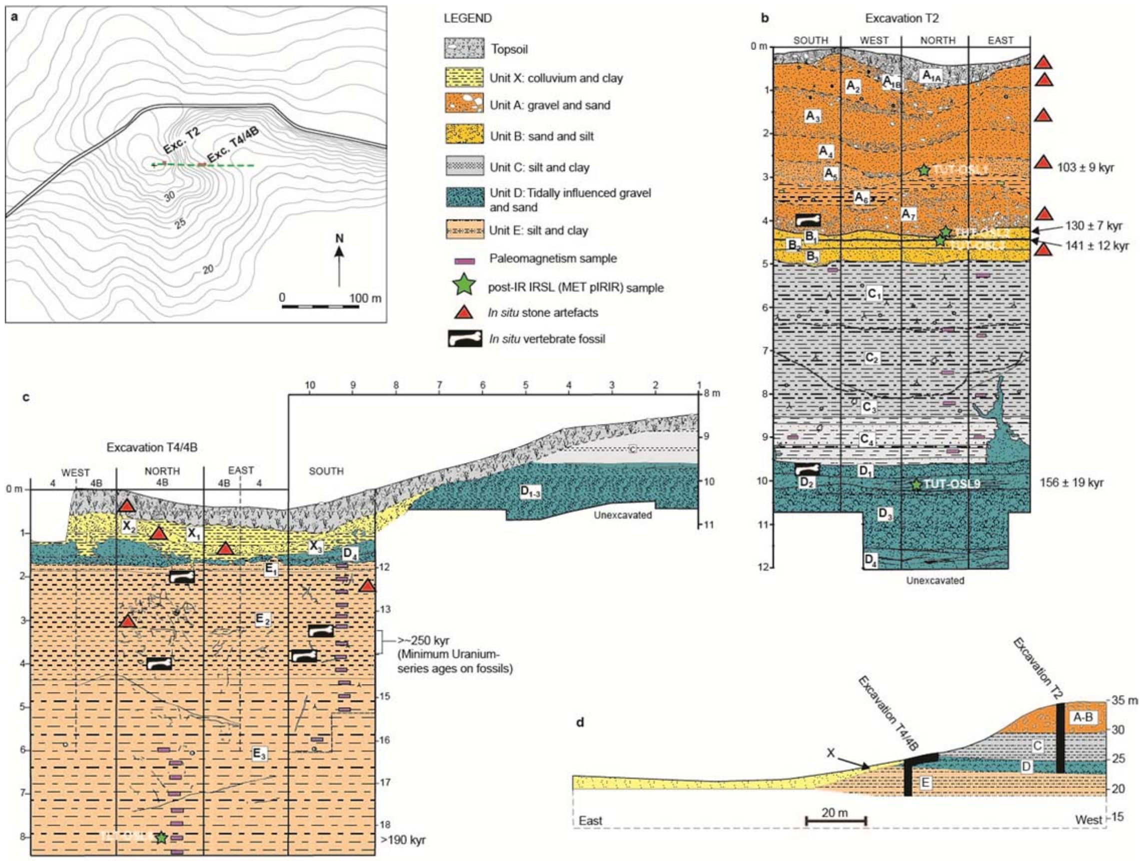

Fig. 2. Plan and stratigraphic profiles for the Talepu excavations. In 2009, we excavated a 2 x 1.5 m trench (T2) to a depth of 10 m near the summit of Talepu hill, where heavily weathered alluvial gravels outcrop over a 70 x 50 m area. To further plumb the stratigraphic depths of the site, we excavated a 9 x 1 m trench (T4) near the foot of the hill 50 m from, and 8.5 metres below, the summit. A 2 x 1 m area of the eastern end of T4 was also continued to a depth of 6.1 metres. T2 and T4 were re-opened in 2012 in order to obtain samples for optical dating and palaeomagnetic analysis, and at this time the trenches were extended vertically to depths of 12 m, and 8.6 m, respectively. **a**, Topographic map of Talepu hill showing the position of excavations T2 and T4. Green dotted line indicates the profile section shown in **d**; **b**, Stratigraphy, fossil and stone artefact occurrences, dating sampling horizons and ages for excavations T2 and T4. Unit A is a conglomerate interval that can be subdivided into seven

distinct layers: A_1, black topsoil with clast-supported gravel and cobbles (heavily weathered); A_2, sandy clay with caliche nodules and few pebbles; A_3, pebbly sand with gravel lag at base; A_4 and A_5, coarse pebbly sand; A_6 silty clay with caliche nodules; A_7, conglomerate. Unit B is a sandy unit subdivided into three layers: B_1, well-sorted, laminated sandy silt to very fine sand, with a thin but distinct silt layer (1 cm) at the base; B_2, medium to fine-grained sand, fining-upward; B_3, well-sorted sand, fining-upward, with small pebbles near the erosive base. Unit C consists of four fine-grained layers: C_1, mottled silty clay with rootlets and caliche nodules; C_2, homogenous silty clay; C_3, heavily mottled silty clay with rootlets and plant remains; C_4, laminated silty clay with sandy streaks; contains poorly preserved plant remains, and an irregular, coarse sandy intrusion in the east baulk. Unit D is a coarse grained interval, characterized by cross-bedded, pebbly and coarse-grained sandy bed-load deposits, which can be subdivided into four layers: D_1, well-sorted pebbly sand with heavy mottling; pebbles have a maximum diameter of 30 mm; D_2, cross-bedded, very coarse sand with rip clasts and isolated small pebbles. Sandy foresets are alternating with 1-10 mm thick mud drapes, indicative of a tidally influenced environment; D_3, clast-supported gravel with clayey rip clasts, with a maximum pebble diameter of 5 cm; D_4, well-sorted medium to fine-grained cross-bedded sand alternating with mud drapes. Unit E is a clayey silt interval, which can be subdivided into three layers: E_1, orange brown clayey silt with grey mottles; E_2, massive greyish brown clayey silts with orange brown mottles and rootlets, containing fossils and stone artefacts; E_3, massive silty clays with buff brown colour, orange brown mottles, caliche nodules and rootlets. In T4 colluvial Unit X rests unconformably on Unit D.

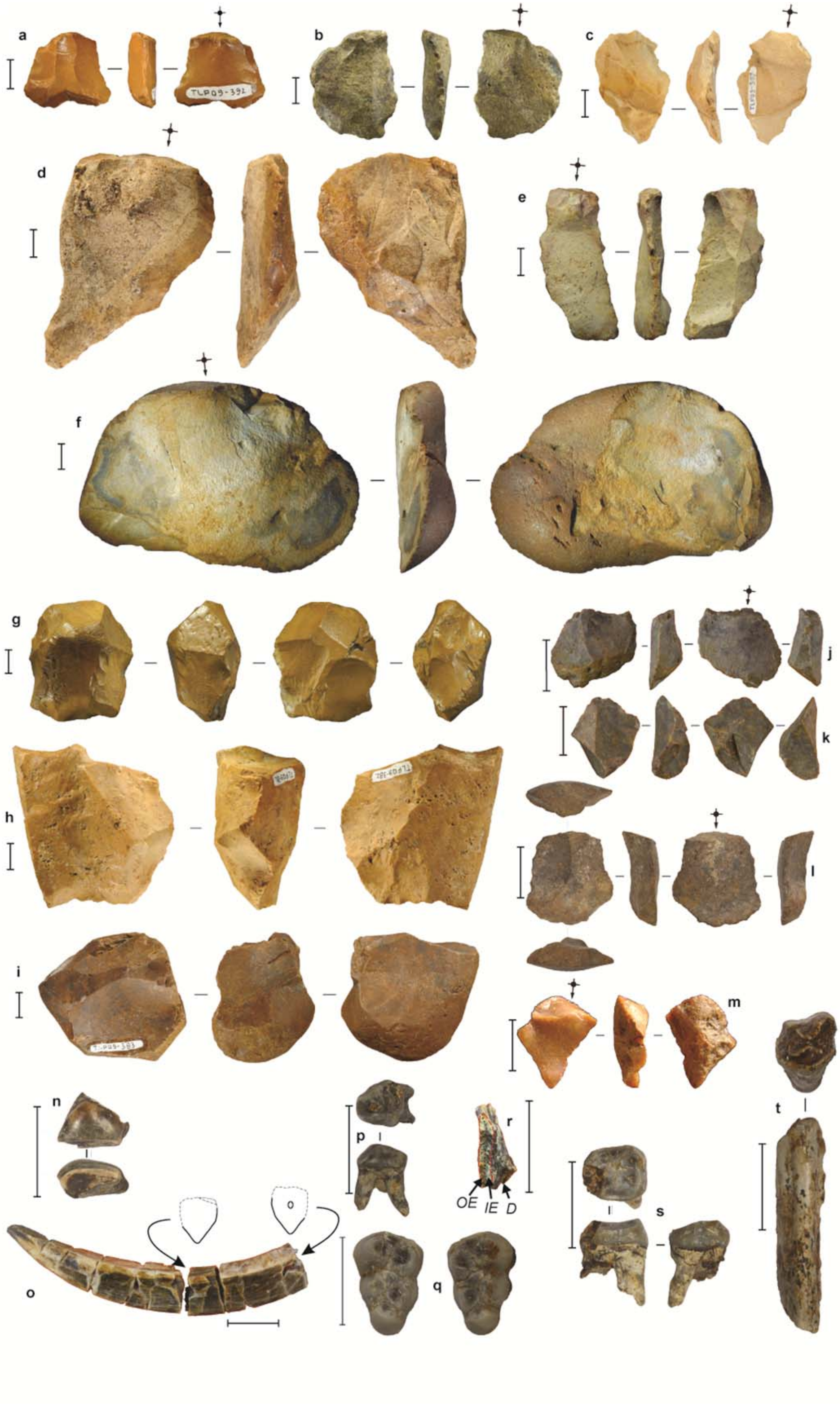
a
TLPQ9-391
b
c
d
e
f
g
h
i
TLPQ9-383
j
k
l
m
n
o
p
q
r
OE
IE
D
s
t

Fig. 3. Stone artefacts and fossil fauna from the Talepu excavations. **a,** flake on silicified limestone (T2, Layer A_7, 3.7-3.8 m depth); **b,** flake on silicified limestone (T2, Layer A_1, 0.4-0.5 m depth); **c,** flake on silicified limestone (T2, Layer A7, 3.6-3.7 m depth); **d,** flake on silicified limestone (T2, Layer A_2, 0.9 m depth); **e,** flake on silicified limestone (T2, Layer A_1, 0.2-0.3 m depth); **f,** pebble flake on silicified limestone (T2 Layer A_2, 0.8-0.9 m depth); **g,** radial core on silicified limestone (T2, Layer A_1, 0.1-0.3 m depth); **h,** core on silicified limestone (T2, Layer A_7, 3.6-3.7 m depth); **i,** core TLP09-383 (T2, Layer A_7, 3.6-3.7 m depth); **j,** silicified limestone flake (T4-B, Layer E_2, 3.0-3.1 m depth); **k,** silicified limestone flake (same material as previous specimen, but does not refit; T4-B, Layer E_2, 3.0-3.1 m depth); **l,** silicified limestone flake (T4, Layer E_2, 2.38 m depth); **m,** silicified limestone flake (T4, Layer E_2, 2.2-2.4 m depth); **n,** left upper incisor of *Celebochoerus* sp. (TLP10-F8*, T4, Layer E_2 3.2-3.4 m depth); **o,** left lower canine of *Celebochoerus* sp. (TLP10-F1*, T4, Layer E2, 3.3 m depth). The cross-section of the canine is of the "*Verrucosus*" type, with the external surface being wider than the posterior surface. The relatively large size of this canine and its long honing surface (indicating that the occluding upper canine was of very large size) suggests it is of *Celebochoerus*, not the still extant suid *Sus celebensis*. In *Babyrousa* the lower canines have a more rounded profile, are devoid of any enamel, and lack honing facets; **p,** right upper p3 of *Celebochoerus* sp. (TLP10-F5, T4 Layer E_2, 3.3-3.4 m depth); **q,** right (TLP10-F3*) and left (TLP10-F4*) upper M3 of *Celebochoerus* sp. (T4, Layer E_2, 3.3-3.4 m depth); **r,** *Stegodon* molar fragment (D = dentine; OE = outer enamel layer; IE = inner enamel layer; both OE and IE are of about equal thickness, which is a diagnostic characteristic of *Stegodon*; TLP12-T4B-F3, T4-B, Layer E_1, 1.9-2 m depth); **s,** upper left p^4 of *Celebochoerus* sp. (TLP10-F2*, T4, Layer E_2, 3.2-3.3 m depth); **t,** lower m_3 fragment of Bovidae, cf. *Bubalus* (Anoa) sp. (TLP09-F2, T2, Layer A_7, 4-4.1 m depth). Specimens marked with '*'

were used for U-Series dating. Scale bars near items a-i represent 10 mm, near items j-t represent 20 mm.

METHODS

1. Excavation methods

In 2007 and 2008 we undertook three (T1-T3) one by two meter test excavations at Talepu Hill, where large numbers of stone artefacts were found scattered on the surface with loose gravel. The summit of Talepu Hill (S 4° 22' 06.5"; E 119° 59' 01.7") lies 36 m above sea level and 18 m above the floodplain of the Walanae River, which flows 600 m to the east (**Fig. 1**). Geological outcrop conditions are very poor, and thick tropical soils cover the underlying geological formations. The three test excavations near the summit of Talepu Hill proved the occurrence of *in situ* stone artefacts down to a depth of at least 1.8 m, in heavily weathered conglomerate lenses and sandy silt layers. The same gravel unit occurs on other hilltops to the west and southwest. At Bulu Palece, 850 m west of Talepu Hill, which is the highest hilltop in the vicinity with an elevation of 51 m (see **Extended Data Fig. 2**), the gravel is at least 13 m thick, but at Talepu Hill only a basal interval of 4.3 m thickness remains.

In October 2009 T2 was taken down to 7 m below surface (**Extended Data Fig. 2c**), at which depth the excavation area was reduced to a 1 x 1 m square and taken down further to a maximum depth of 10 m. To ensure that this deep-trench operation was undertaken safely, we installed timber shoring as the work progressed. A new east-west oriented, 1 x 9 m trench (T4) was excavated at the base of the Talepu hill, 40 m east of T2. This trench reached a maximum depth of 2 m, revealing the lateral development of the stratigraphy near the base of the hill (**Fig. 2**). Deposits were removed in 10 cm spits within stratigraphic units. Stone artefacts and fossils found by the excavators were bagged and labelled immediately; all other deposits were dry sieved with 5 mm mesh to separate out clasts, including stone artefacts. Pebbles from each spit were weighed; and composition analysis was undertaken on clasts from a representative sample from 6 spits: average maximum clast diameter was recorded by measuring the longest diameter of the 10 largest clasts per spit (**Extended Data Fig. 3**). Bulk samples of stratigraphic units were taken for sediment and pollen analyses.

In October 2010, the excavations at Talepu were continued. An 1 x 2 m area at the east end of T4 was excavated to a depth of 6.20 m below the surface (**Extended Data Fig. 2d**), thus providing an additional 6 m stratigraphically below the section covered by Excavation 2 in 2009. The T4 deposits were removed in 20 cm spits within stratigraphic units. Following the excavation of an *in situ* stone artefact (Specimen S-TLP10-1, a flake from Layer E_2 at a depth of 2.28 m below the surface) and fossils of *Celebochoerus*, it was decided to wet-sieve all the excavated sediments with 3 mm mesh to separate out stones and other clasts, including stone artefacts. Wet-sieving of the silty clay deposits from the interval between 2 and 2.4 m depth yielded two more stone artefacts (S-TLP10-2 and S-TLP10-4) and one possible stone artefact (S-TLP10-3).

In October 2012 backfill of T2 and T4 was removed. T4 was enlarged with a 1 x 2 m extension (T4-B), and both T2 and T4/4B were taken further down with an additional 2 m and 2.1 m, respectively, in order to allow for sampling for palaeomagnetic and optical dating methods.

2. Uranium-series dating

The details for laser ablation U-series analysis of skeletal materials were recently summarised[31]. U-series analyses provide insights into when U migrates into a bone or tooth. This may happen a short time after the burial of the skeletal element or some significant time span later. There may also be later U-overprints that are difficult to recognise. As such, apparent U-series results from faunal remains have generally to be regarded as minimum age estimates. It is very difficult or impossible to evaluate by how much the U-series results underestimate the correct age of the sample. Details of the instrumentation, analytical procedures and data evaluation have been modified from those described in detail elsewhere[16,31]. All isotope ratios refer to activity ratios.

Sequential laser spot analyses were undertaken on cross sections of eight *Celebochoerus* fossils from the T4 excavation at Talepu. They comprised fragments of six teeth and two bones from Layer E_2 found up to 60 cm below the lowest stone artefacts in the same silty clay layer. Of one fossil (TLP10-1, a *Celebochoerus* lower canine), two subsamples were analysed (a and b). Each fossil specimen was cut transversely using a dentist drill with a diamond saw blade (**Extended Data Fig. 5**). Four to five samples were then mounted together into alluminium cups, aligning the cross-sections with the outer rim of the sample holder, which later positions the samples on the focal plane of the laser. U-series isotopes were measured using the laser ablation MC-ICP-MS system at The Australian National University's (ANU) Research School of Earth Sciences. It consists of a Finnigan MAT Neptune MC-ICP-MS equipped with multiple Faraday cups. At the time of measurement, the mass spectrometer had only one ion counter. This necessitated two sequential sets of measurements along parallel tracks, one for ^{230}Th and a second for ^{234}U. The ion counter was set either to mass of 230.1 or 234.1 while the Faraday cups measured the masses 232, 235, and 238. Samples were ablated with a Lambda Physik LPFPro ArF excimer (λ=193 nm) laser coupled to the Neptune through an ANU-designed Helex ablation cell.

The samples were initially cleaned for 10 s with the laser spot size set to 265 µm followed by a 50 s analysis run with a 205 µm spot size using a 5 Hz pulse rate. Analyses were carried out at regular intervals along traverses, all starting from the exterior surface (**Extended Data Fig. 5**). The data sets of each transect were bracketed between reference standard analyses to correct for instrument drift.

Semi-quantitative analysis of U and Th concentrations were derived from repeated measurements of the SRM NIST-610 glass (U = 461.5 µg/g; Th = 457.2 µg/g), and U-isotope ratios from repeated measurements of rhinoceros tooth dentine from Hexian (sample 1118)[32]. Age estimates combining all measurements on a specimen were calculated using the iDAD program[17], assuming diffusion from both surfaces for the bones (TLP10-6 and 7) and roots of the teeth (**Extended Data Fig. 5a-h**) and directional diffusion from the central pulp cavity into the dentine and covering enamel for TLP10-9 (**Extended Data Fig. 5i**). The enamel data of the latter sample were omitted as enamel has a different diffusion rate. Generally, results with elemental U/Th < 300 are rejected, as these are associated with detrital contamination. However, this applied only to a single measurement. The finite ages are given with 2-σ error bands, the infinite results only refer to the lower bound of the 2-σ confidence interval (**Supplementary Table 1**). None of the samples showed any indication for U-leaching, which is either expressed by sections with 230Th/234U >> 234U/238U or increasing 230Th/234U ratios towards the surface in conjunction with decreasing U-concentrations.

Five samples had infinite positive error bounds and it was thus only possible to calculate minimum ages. It can be seen that the U-series results may change over small distances within a sample. The first data set of TLP10-1 yielded a finite result of 161±15 kyr while the second set yielded a minimum age of > 255 kyr. As mentioned above, all U-series results, whether they are finite of infinite, have to be regarded as minimum age estimates. Provided that the faunal elements present a single population, the U-series results indicate that the Talepu samples are most likely older than ~350 kyr. (**Supplementary Table I**). The large errors do not allow us to further constrain the age.

3. Optical dating

Optical dating provides an estimate of the time since grains of quartz or potassium (K)-rich feldspar were last exposed to sunlight[33-35]. The burial age is estimated by dividing the equivalent dose (D_e, a measure of the radiation energy absorbed by grains during their period of burial) by the environmental dose rate (the rate of supply of ionising radiation to the grains over the same period). The D_e is determined from the laboratory measurements of the optically stimulated luminescence (OSL) signals from quartz or the infrared (IR) stimulated luminescence (IRSL) from K-feldspar, and the dose rate is estimated from laboratory and field measurements of the environmental radioactivity.

K-feldspar has two advantages over quartz in optical dating: (1) the IRSL signal (per unit absorbed dose) is usually much brighter than the OSL signal from quartz and (2) the IRSL traps saturate at a much higher dose than the OSL traps, which makes it possible to date samples older than 200 ka (the typical limit for quartz). However, the routine dating of K-feldspars using the IRSL signal has been hampered by the malign phenomenon of 'anomalous fading' (i.e., the leakage of electrons from IRSL traps at a faster rate than expected from kinetic considerations), which gives rise to substantial underestimates of age unless an appropriate correction is made[36,37]. Only recently have IRSL traps that are less prone to fading been identified[38], using either a post-IR IRSL (pIRIR) approach[39,40] or a multiple-elevated-temperature (MET) pIRIR procedure[41,42]. Reference [43] reviews the progress, potential and remaining problems in using these pIRIR signals for dating.

Dating the samples from Talepu using quartz OSL is impractical because of the paucity of quartz. Furthermore, the quartz OSL traps are expected to be in saturation owing to the ages of the samples (>100 ka) and the high environmental dose rates of the deposits (4–5 Gy/ka). In this study, we applied the MET-pIRIR procedure to K-feldspar extracts from Talepu to isolate the light-sensitive IRSL signal that is least prone to anomalous fading. We also allowed for any residual dose at the time of sediment deposition, to account for the fact that pIRIR traps are less easily bleached than the 'fast' component OSL traps in quartz. The resulting MET-pIRIR ages should, therefore, be reliable estimates of the time of sediment deposition.

3.1. Sample collection

Sediment samples were collected by hammering opaque plastic tubes (5 cm in diameter) into the cleaned section faces of the Talepu Upper Trench (TUT) and Talepu Lower Trench (TLT) excavations. The tubes were removed and wrapped in light-proof plastic for transport to the Luminescence Dating Laboratory at the University of Wollongong. Additional bags of sediment were collected from the tube holes and sealed in zip-lock plastic bags for laboratory measurements of sample radioactivity and field water content. A portable gamma-ray spectrometer was inserted into each of the tube holes and replicate measurements were made of the *in situ* gamma dose rate at each sample location.

Under dim red laboratory illumination, each sample was treated using standard procedures to extract sand-sized grains of K-feldspar[34]. The samples were treated with hydrochloric acid and hydrogen peroxide solutions to remove carbonates and organic matter, and then dried. Grains of 90–180 or 180–212 µm in diameter were obtained by dry sieving. The K-feldspar grains were separated from quartz and heavy minerals using a sodium polytungstate solution of density 2.58 g/cm^3, and etched in 10% hydrofluoric acid for 40 minutes to clean the surfaces of the grains and to reduce the alpha-irradiated layer around the surface of each grain.

IRSL measurements were made on an automated Risø TL-DA-20 reader equipped with IR diodes (875 Δ 40 nm) for stimulation, which delivered a total power of ~135 mW/cm^2 to the sample position[44]. Irradiations were carried out within the reader using a calibrated ^{90}Sr/^{90}Y beta source. The IRSL signals were detected using an Electron Tubes Ltd 9235B photomultiplier tube, with the stimulated luminescence passing through a filter pack containing Schott BG-39 and Corning 7-59 filters to provide a blue transmission window (320–480 nm). Aliquots containing several hundred grains were prepared by mounting the grains as a ~5 mm-diameter monolayer in the centre of a 9.8 mm-diameter stainless steel disc, using “Silkospray” silicone oil as the adhesive.

3.2. Environmental dose rates

Dose rates were determined from field measurements of the gamma dose rate, laboratory measurements of the beta dose rate (using the sediment samples recovered from each tube hole), and published estimates of the cosmic-ray dose rate and the internal dose rate (due to ^{40}K and ^{87}Rb contained within the K-feldspar grains). The total dose rate, therefore, consists of 4 components: the external gamma, beta and cosmic-ray dose rates, and the internal beta dose rate. The dosimetry data for all samples are summarised in **Supplementary Table 2**.

The external gamma dose rates were measured using an Exploranium GR-320 portable gamma-ray spectrometer, which is equipped with a 3-inch diameter NaI(Tl) crystal calibrated for U, Th and K concentrations using the CSIRO facility at North Ryde[45]. At each sample location, 3–4 measurements of 300 s duration were made of the gamma dose rate at field water content. The external beta dose rate was measured by low-level beta counting using a Risø GM-25-5 multicounter system[46] and referenced to the Nussloch Loess (Nussi) standard, with allowance made for the effect of grain size and hydrofluoric acid etching on beta-dose attenuation. These external components of the total dose rate were adjusted for assumed long-term water contents of 20% for the TUT samples and 30% for the TLT sample. These values are based on the measured field water contents (see **Supplementary Table 2**), together with an assigned 1σ uncertainty of ± 5% to capture the likely range of time-averaged values over the entire period of sample burial.

The minor contribution from cosmic rays was estimated from the burial depths of the samples and the latitude, longitude and altitude of the Talepu sites[47], with adjustment for water content[48]. The internal dose rate was estimated by assuming ^{40}K and ^{87}Rb concentrations of 13 ± 1% and 400 ± 100 ppm, respectively[49-52].

To check the equilibrium status of the ^{238}U and ^{232}Th decay chains, samples TUT-OSL2 and TUT-OSL3 were analysed by high-resolution gamma-ray spectrometry (HRGS). The measured activities of ^{238}U, ^{226}Ra and ^{210}Pb in the ^{238}U series, ^{228}Ra and ^{228}Th in the ^{232}Th series, and ^{40}K are listed in **Supplementary Table 3**. The activities of ^{228}Ra and ^{228}Th are close to equilibrium for both samples, as is commonly the case with the ^{232}Th series. The ^{238}U chain, however, shows evidence of substantial disequilibrium at the present day. Sample TUT-OSL2 has a 39–45% deficit of ^{226}Ra and ^{210}Pb relative to the parental ^{238}U activity, whereas sample TUT-OSL3 has a 224–345% excess of the daughter nuclides.

Sample TUT-OSL3 is from a sandy layer (Layer B) through which ground water can percolate, so we attribute the ^{226}Ra excess in this sample to the deposition of radium transported by ground water. Given the similar ^{238}U activities in TUT-OSL2 and TUT-OSL3, it is reasonable to assume that the parental uranium activity has not changed substantially during the period of burial of either sample, and that the ^{226}Ra excess in TUT-OSL3 most likely occurred recently. The latter can be deduced from the fact that ^{226}Ra has a half-life of ~1600 years, which is short relative to the ages of our samples (>100 ka), so any unsupported excess of ^{226}Ra would have decayed back into equilibrium with ^{238}U within ~8000 years of deposition (i.e., 5 half-lives of ^{226}Ra). The alternative option – that groundwater has continuously supplied excess ^{226}Ra to Layer B – is not supported by the disequilibrium between ^{226}Ra and ^{210}Pb: the latter nuclide has a half-life of ~22 years, so it should remain in equilibrium with ^{226}Ra if the latter is supplied continuously and no radon gas is lost to atmosphere. Moreover, as the return of ^{210}Pb to equilibrium with ^{226}Ra is governed by the half-life of the shorter-lived nuclide, it could be argued that the excess ^{226}Ra was deposited within the last ~110 years (5 half-lives of ^{210}Pb).

Fortunately, the calculated age of TUT-OSL3 is not especially sensitive to different assumptions about the timing or extent of disequilibria in the ^{238}U series. The latter accounts for only 28% of the total dose rate estimated from the HRGS data in **Supplementary Table**

3; this assumes that the present-day nuclide activities have prevailed throughout the period of sample burial. But if instead, as we consider more likely, the observed excess in ^{226}Ra was deposited recently and the ^{238}U decay chain has been in equilibrium for most of the period of sample burial, then the ^{238}U series accounts for only 12% of the total dose rate (i.e., using activities of 37 ± 4 Bq/kg for ^{238}U, ^{226}Ra and ^{210}Pb). The ages calculated under these two alternative scenarios using the HRGS data range from ~118 to ~143 ka (**Supplementary Table 3**).

Sample TUT-OSL2 is from the more silty overlying layer (Layer A_7) and has deficits of ^{226}Ra and ^{210}Pb relative to ^{238}U, but the magnitude of these disequilibria is much smaller than those in TUT-OSL3. If it were not continuously leached from the sample, ^{226}Ra will return to secular equilibrium with ^{238}U within ~8000 years, so the existence of disequilibrium in TUT-OSL2 adds further weight to the argument for recent transport of ^{226}Ra in ground water at Talepu. The alternative is that ^{226}Ra has been leached continuously from this sample, so we carried out the same sensitivity test on the dose rates and ages as that performed on TUT-OSL3. For TUT-OSL2, the ages determined using the present-day HRGS data or activities of 41 ± 3 Bq/kg for ^{238}U, ^{226}Ra and ^{210}Pb are statistically indistinguishable (127 and 122 ka, respectively, each with a 1σ uncertainty of ± 11 ka; **Supplementary Table 3**), owing to the fact that the disequilibria are much less marked than in TUT-OSL3 and the ^{238}U series makes only a small contribution (10–14%) to the total dose rate of TUT-OSL2.

For purposes of calculating the ages of the Talepu samples, we used the beta dose rates deduced from direct beta counting and the *in situ* gamma dose rates measured in the field. The latter take into account the spatial heterogeneity in dose rate derived from the ~30 cm of deposit surrounding each sample, and is based on the present-day nuclide activities (with that of ^{214}Bi, a short-lived nuclide between ^{226}Ra and ^{210}Pb, being used for the ^{238}U series). The beta dose rates determined from beta counting and from the measured HRGS data (**Supplementary Table 3**) are similar for both TUT-OSL2 (~2.0 and ~2.2 Gy/ka) and TUT-OSL3 (~2.5 and ~2.7 Gy/ka); such agreement is expected, as both measure the present-day activities. The *in situ* gamma dose rate for TUT-OSL2 (~1.6 Gy/ka) is also similar to that calculated from the HRGS data, whether the ^{238}U activity is applied to the daughter products (~1.4 Gy/ka) or the measured daughter activities are used instead (~1.5 Gy/ka). The *in situ* gamma dose rate of ~1.3 Gy/ka for TUT-OSL3 is similar to the HRGS estimate obtained using the ^{238}U activity for ^{226}Ra and ^{210}Pb (~1.4 Gy/ka), but is lower than that calculated from the measured daughter activities (~2.0 Gy/ka). This difference might appear counter-intuitive as the latter reflects the present-day nuclide activities in the sample, but the lower field gamma dose rate is compatible with the location of TUT-OSL3 close to the boundary with the TUT-OSL2 sediments, which have a beta dose rate ~20% smaller (**Supplementary Table 2**). Furthermore, the observation that the *in situ* gamma dose rate for TUT-OSL3 is lower than that estimated from the HRGS measurements indicates that the excesses of ^{226}Ra and ^{210}Pb are spatially localised and are not pervasive in the 30 cm of deposit surrounding this sample.

3.3. MET-pIRIR measurements

The single-aliquot regenerative dose (SAR) MET-pIRIR procedure introduced by Li and Li[41] was adapted for the Talepu samples. With this procedure, the IRSL signals of both the regenerative and test doses are measured by increasing the stimulation temperature from 50 to 250 °C in steps of 50 °C. In this study, we modified the original procedure by using a preheat at 320 °C (rather than 300 °C) for 60 s, to avoid significant influence from residual phosphorescence while recording the MET-pIRIR signal at 250 °C. In addition, following reference 53, we used a 2 hr solar simulator bleach before each regenerative dose cycle, instead of the high-temperature IR bleaching step used in the conventional procedure. We found that introducing a solar simulator bleach is essential to recover a known dose given in the laboratory, as discussed below. A step-by-step guide to the modified procedure used in this study is shown in **Supplementary Table 4**.

3.3.1 Decay curves and dose-response curves

Extended Data Figure 6a shows typical IRSL and MET-pIRIR decay curves for an aliquot of sample TUT-OSL2. The decay curves observed at the different stimulation temperatures are similar in shape, with initial MET-pIRIR signal intensities on the order of a few thousand counts per second. **Extended Data Figure 6b** shows representative dose-response curves for the same aliquot. Each sensitivity-corrected (L_x/T_x) dose-response curve (DRC) was fitted using a single saturating-exponential function of the following form:

$$I = I_0 (1 - \exp^{-D/D_0})$$

where I is the L_x/T_x value at regenerative dose D, I_0 is the saturation value of the exponential curve and D_0 is the characteristic saturation dose. The D_0 values are shown next to each DRC in **Extended Data Figure 6b**. Similar results were observed for different aliquots from the five Talepu samples examined. The DRCs show that, for these samples, natural doses of up to ~800 Gy can be measured reliably using the MET-pIRIR signals.

3.3.2 Residual doses

To validate whether the MET-pIRIR procedure is applicable to the Talepu samples, we conducted several tests, including dose recovery, anomalous fading and residual dose tests. For the latter, 4 aliquots of each sample were bleached for 4–5 hr using a Dr Hönle solar simulator (model UVACUBE 400). The residual doses were then estimated by measuring these bleached aliquots using the MET-pIRIR procedure in **Supplementary Table 4**. The residual doses obtained for each of the TUT samples are plotted against stimulation temperature in **Extended Data Figure 7a**. The IRSL signal measured at 50 °C has a few Gy of residual dose, and this increases as the stimulation temperature is raised, attaining values of 16–20 Gy at 250 °C. The size of the residual dose is only about 2–3% of the corresponding D_e values for the 250 °C signal, and these were subtracted from the D_e values for the respective samples before calculating their ages.

Reference 54 noted that a simple subtraction of the residual dose from the apparent D_e value could result in underestimation of the true D_e value if the residual signal is large relative to the bleachable signal. They advocated the use of an intensity-subtraction procedure instead of the simple dose-subtraction approach for samples with large residual doses. The dose-subtraction approach, however, should be satisfactory for the Talepu samples, given the small size of the residual dose compared to the D_e values obtained from the MET-pIRIR 250 °C signal.

3.3.3 Dose recovery tests

A dose recovery test[55] was conducted on sample TUT-OSL1. Eight aliquots were bleached by the solar simulator for 5 hr, and then given a dose of 550 Gy. Four of these aliquots were measured using the conventional MET-pIRIR method[41], with a 'hot' IR bleach of 320 °C for 100 s applied at the end of each SAR cycle (step 15 in **Supplementary Table 4**). The other 4 aliquots were measured using the modified MET-pIRIR procedure (**Supplementary Table 4**), with a solar simulator bleach of 2 hr used at step 15. The measured doses at each stimulation temperature were then corrected for the corresponding residual doses (**Extended Data Fig. 7a**), and the measured/given dose ratios calculated for the various IRSL and MET-pIRIR signals. The dose recovery ratios are plotted in **Extended Data Figure 7b**, which shows that a hot IR bleach at the end of each SAR cycle results in significant overestimation of the known (given) dose; for example, up to ~48% overestimation is observed for the MET-pIRIR 250 °C signal.

A 'recycling ratio' consistent with unity (1.00 ± 0.05) was obtained for two duplicate regenerative doses given to this sample as part of the SAR procedure, using the hot IR bleach at step 15. This ratio indicates that the sensitivity correction (using the test dose signals) worked successfully between the regenerative-dose cycles. The overestimation in recovered dose, therefore, implies the failure of the sensitivity correction for the natural dose – that is, the extent of sensitivity change between the natural dose and its corresponding test dose measurement is different from the changes that occur between the subsequent regenerative doses and their corresponding test dose measurements. As the only difference between the natural and regenerative dose measurements is the preceding bleaching treatment (i.e., the natural dose was applied after a solar simulator bleach, whereas the regenerative doses were measured after a hot IR bleach), we decided to test the effect of applying a solar simulator bleach at the end of each regenerative-dose cycle (step 15). **Extended Data Figure 7b** shows that the dose recovery results improved significantly using this modified procedure, with all of the measured/given dose ratios consistent with unity at 2σ for the signals measured at different temperatures; a ratio of 1.02 ± 0.06 was obtained for the MET-pIRIR 250 °C signal.

The dose recovery test results for sample TUT-OSL1 suggest that the MET-pIRIR procedure can successfully recover a known dose given to K-feldspars from Talepu, but only when a solar simulator bleach is applied at the end of each SAR cycle. We therefore adopted this procedure to measure the D_e values for all five Talepu samples.

3.3.4 Anomalous fading tests

Previous studies of pIRIR signals have shown that the anomalous fading rate (*g*-value) depends on the stimulation temperature, with negligible fading of MET-pIRIR signals stimulated at temperatures of 200 °C and above[41]. Accordingly, no fading correction is required for these high-temperature MET-pIRIR signals (see review by Li *et al.*[43]). To demonstrate this applies also to the Talepu samples, fading tests were conducted on 6 aliquots of sample TUT-OSL3 that had already been used for D_e measurements. We adopted a single-aliquot procedure similar to that described by Auclair *et al.*[56], but based on the MET-pIRIR procedure. Doses of 110 Gy were administered using the laboratory beta source, and the irradiated aliquots were then preheated and stored for periods of up to 1 week at room temperature. For practical reasons, a hot IR bleach (320 °C for 100 s) was used instead of a solar simulator bleach at the end of each SAR cycle, but this choice should not affect the outcome of the fading test, given the aforementioned recyling ratio of unity obtained with the hot IR bleach.

The fading rates (*g*-values) were calculated for the different IRSL and MET-pIRIR signals and normalised to the time of prompt measurement of the IRSL signal (1500 s). These data are plotted in **Extended Data Figure 8a** and show that the highest fading rate is observed for the 50 °C IRSL signal (4.9 ± 0.3 %/decade). The *g*-values decrease as the stimulation temperature is increased, falling to 0.92 ± 0.86 and 0.17 ± 1.09 %/decade for the 200 and 250 °C signals, respectively. These results suggest that the MET-pIRIR 250 °C signal fades negligibly in the Talepu samples, so we have used the D_e values obtained from this signal to estimate the final ages.

3.3.5 D_e measurements

Based on the above performance tests, the MET-pIRIR procedure in **Supplementary Table 4** was used to estimate the D_e values for the TUT samples. Those obtained from the MET-pIRIR 250 °C signal are displayed as radial plots in **Extended Data Figure 8b**. In such plots, the most precise estimates fall to the right and the least precise to the left. If these independent estimates are statistically consistent with a common D_e value, then 95% of the points should scatter within a band of width ± 2 units projecting from the left-hand ('standardised estimate') axis to the common D_e value on the right-hand, radial axis. The radial plot thus provides simultaneous information about the spread, precision and statistical consistency of D_e values[55,57,58]. Most of the D_e values in **Extended Data Figure 8b** are distributed around a central value, although the spread in D_e values is larger than can be explained by the measurement uncertainties alone. The overdispersion (OD) among these D_e values is ~20% for three of the TUT samples and almost twice this amount for TUT-OSL9, the latter arising from a pair of low D_e values measured with relatively high precision. To estimate the age for each of these samples, we determined the weighted mean D_e of the individual single-aliquot values using the Central Age Model (CAM) of Galbraith *et al.*[55], which takes account of the measured OD in the associated standard error.

To further test the reliability of our D_e estimates for the TUT samples, the CAM estimates are plotted as a function of stimulation temperature in **Extended Data Figure 9a**. Such plots show how the ages increase with an increase in stimulation temperature until a plateau is reached at higher temperatures; the plateau (shown as a dashed line) indicates that a non-fading component is present at these elevated temperatures. The age plateau can be used, therefore, as a internal diagnostic tool to check that a stable, non-fading component has been isolated for age determination. For all four TUT samples, a plateau is reached at temperatures above 200 °C, so our final ages are based on the D_e values obtained from the non-fading MET-pIRIR 250 °C signal. The corresponding weighted mean D_e values, dose rate data and final ages are listed in **Supplementary Table 2**.

We also measured one sample (TLT-OSL6) collected from near the base of the stratigraphically underlying deposits in the Lower Trench. Four of the 8 aliquots measured from this sample emitted natural MET-pIRIR 250 °C signals consistent with the saturation levels of the corresponding DRC (e.g. **Extended Data Figure 9b**), implying that the IRSL traps are saturated in the natural sample. It would be hazardous to estimate the age of TLT-OSL6 from the D_e values of the 4 non-saturated aliquots, as these may represent only the low D_e values in the 'tail' of a truncated distribution. The saturation dose of the MET-pIRIR 250 °C signal places an upper limit on reliable D_e estimation of ~800 Gy for this sample. We conclude, therefore, that TLT-OSL6 has a D_e of more than 800 Gy, which corresponds to a minimum age of ~190 ka (**Supplementary Table 2**).

3.4. K-feldspar chronology

The MET-pIRIR 250 °C ages for the four samples dated from the Upper Trench are in correct stratigraphic order, increasing from 103 ± 9 ka (at ~3 m depth) to 156 ± 19 ka (at ~10 m depth). They thus span the period from Marine Isotope Stage (MIS) 6 – the penultimate glacial – to MIS 5, the last interglacial. This coherent sequence of ages also supports our contention that the Talepu samples were sufficiently bleached prior to deposition.

The single sample analysed from ~8 m depth in the Lower Trench (TLT-OSL6) yielded a minimum age of ~190 ka, corresponding to MIS 7 (the penultimate interglacial) or earlier. We have not yet dated the overlying sediments in the Lower Trench, but we expect the lower 6 m of exposed deposits to be older than 156 ± 19 ka, as they stratigraphically underlie sample TUT-OSL9 in the Upper Trench.

4. Palaeomagnetic Dating

Samples for palaeomagnetic polarity assessment were taken from the baulks of excavations Talepu 2 (T2) and Talepu 4 (T4) (**Fig. 2**). Samples were taken at 20-30 cm intervals using non-magnetic tools. Preferrably samples in non-bioturbated silty deposits were taken. The upper conglomeratic interval of T2 was omitted because of its coarser grain-size and because it appeared heavily affected by soil formation and plant root bioturbation. From each sample level five oriented sample specimens were retrieved by carving the sediment using non-magnetic tools and fitting it into 8 cm^3 plastic cubes. The samples were labelled according to excavation, baulk and depth.

In the laboratory all specimens were treated by an Alternating Field (AF) demagnetizer. Demagnetization was performed with intervals of 2.5 – 5 mT to a peak of up to 80-1000 mT. The magnetization vectors obtained from most samples showed no more than two separated components of NRM on the orthogonal planes, which means that the specimens had been affected by secondary magnetization. However, secondary magnetization was easily removed with a demagnetization of up to 5-20 mT, while the Characteristic Remanent Magnetizations (ChRMs) could be isolated through stepwise demagnetization of up 20-40 mT, in some cases up to 50 mT. Above 40 mT most samples were completely demagnetized (**Extended data Fig.3e**). The mean magnetic directions for each sample are presented in **Supplementary Table 5**.

The mean magnetisation intensities and palaeomagnetic directions are plotted against stratigraphic depth in **Extended Data Figure 4**. The 90 – 98 % intensity saturation was achieved from between 1.30×10^{-4} A/m to 3.81×10^{-3} A/m before demagnetization, and between 8.52×10^{-6} A/m to 1.49 x 10-4 A/m after demagnetization at 20-40 mT. The direction of ChRMs is determined from the orthogonal plots in at least four to five successive measurement steps between 20 to 50 mT using the principal component analysis[59] (PuffinPlot[60] and IAPD 2000 software[61]) with the maximum angular deviations setting at < 5°. Although there are no well-defined criteria for the acceptability of palaeomagnetic data available, the $k > 30$ and $\alpha95 < 15°$ criterium of reference 62 was used to accept the average remanence direction for sampled levels. Based on these tests, all the samples (N=24) throughout the Talepu sequences yielded acceptable and significant ChRMs directions and show a Normal Polarity. The ChRMs directions are relatively constant throughout the sequences, except the direction of samples taken at 6 and 7 m depth, which show steep inclinations of up to 50 - 60°. Such steep inclinations are unusual for near-equatorial regions.

One possible interpretation is that post depositional mass-movement disturbances, such as creep or a landslide resulted in rotational movements of this interval.

The equal area projections show that the dispersion of within site means of the remanence directions are regrouping more closely together after demagnetization, and no significant change in the major remanence direction occurs with depth. The major remanent direction corresponds closely with the present magnetization direction (**Extended Data Figure 4b**).

References

31 Grün, R., Eggins, S., Kinsley, L., Moseley, H. & Sambridge, M. Laser ablation U-series analysis of fossil bones and teeth. *Palaeogeography, Palaeoclimatology, Palaeoecology* **416**, 150-167 (2014).

32 Grün, R. *et al.* ESR and U-series analyses of teeth from the palaeoanthropological site of Hexian, Anhui Province, China. *Journal of Human Evolution* **34**, 555-564 (1998).

33 Huntley, D. J., Godfrey-Smith, D. I. & Thewalt, M. L. Optical dating of sediments. (1985).

34 Aitken, M. J. *An introduction to optical dating: the dating of Quaternary sediments by the use of photon-stimulated luminescence*. (Oxford University Press, 1998).

35 Lian, O. B. & Roberts, R. G. Dating the Quaternary: progress in luminescence dating of sediments. *Quaternary Science Reviews* **25**, 2449-2468 (2006).

36 Wintle, A. G. Anomalous fading of thermo-luminescence in mineral samples. *Nature* **245**, 143-144 (1973).

37 Huntley, D. J. & Lamothe, M. Ubiquity of anomalous fading in K-feldspars and the measurement and correction for it in optical dating. *Canadian Journal of Earth Sciences* **38**, 1093-1106 (2001).

38 Thomsen, K. J., Murray, A., Jain, M. & Bøtter-Jensen, L. Laboratory fading rates of various luminescence signals from feldspar-rich sediment extracts. *Radiation measurements* **43**, 1474-1486 (2008).

39 Buylaert, J.-P., Murray, A., Thomsen, K. J. & Jain, M. Testing the potential of an elevated temperature IRSL signal from K-feldspar. *Radiation measurements* **44**, 560-565 (2009).

40 Thiel, C. *et al.* Luminescence dating of the Stratzing loess profile (Austria) – testing the potential of an elevated temperature post-IR IRSL protocol. *Quaternary International* **234**, 23-31 (2011).

41 Li, B. & Li, S.-H. Luminescence dating of K-feldspar from sediments: a protocol without anomalous fading correction. *Quaternary Geochronology* **6**, 468-479 (2011).

42 Li, B. & Li, S.-H. Luminescence dating of Chinese loess beyond 130 ka using the non-fading signal from K-feldspar. *Quaternary Geochronology* **10**, 24-31 (2012).

43 Li, B., Jacobs, Z., Roberts, R. G. & Li, S.-H. Review and assessment of the potential of post-IR IRSL dating methods to circumvent the problem of anomalous fading in feldspar luminescence. *Geochronometria* **41**, 178-201 (2014).

44 Bøtter-Jensen, L., Andersen, C., Duller, G. & Murray, A. Developments in radiation, stimulation and observation facilities in luminescence measurements. *Radiation measurements* **37**, 535-541 (2003).

45 Hutton, J. & Prescott, J. Field and laboratory measurements of low-level thorium, uranium and potassium. *International Journal of Radiation Applications and*

Instrumentation. Part D. Nuclear Tracks and Radiation Measurements **20**, 367-370 (1992).

46 Bøtter-Jensen, L. & Mejdahl, V. Assessment of beta dose-rate using a GM multi-counter system. *Nuclear Tracks and Radiation Measurements* **14**, 187-191 (1988).

47 Prescott, J. & Hutton, J. T. Cosmic ray contributions to dose rates for luminescence and ESR dating: large depths and long-term time variations. *Radiation measurements* **23**, 497-500 (1994).

48 Readhead, M. Thermoluminescence dose rate data and dating equations for the case of disequilibrium in the decay series. *International Journal of Radiation Applications and Instrumentation. Part D. Nuclear Tracks and Radiation Measurements* **13**, 197-207 (1987).

49 Huntley, D. & Baril, M. The K content of the K-feldspars being measured in optical dating or in thermoluminescence dating. *Ancient TL* **15**, 11-13 (1997).

50 Huntley, D. & Hancock, R. The Rb contents of the K-feldspar grains being measured in optical dating. *Ancient TL* **19**, 43-46 (2001).

51 Zhao, H. & Li, S.-H. Internal dose rate to K-feldspar grains from radioactive elements other than potassium. *Radiation measurements* **40**, 84-93 (2005).

52 Li, B., Li, S.-H., Wintle, A. G. & Zhao, H. Isochron dating of sediments using luminescence of K‐feldspar grains. *Journal of Geophysical Research: Earth Surface (2003–2012)* **113** (2008).

53 Li, B., Roberts, R. G., Jacobs, Z. & Li, S.-H. A single-aliquot luminescence dating procedure for K-feldspar based on the dose-dependent MET-pIRIR signal sensitivity. *Quaternary Geochronology* **20**, 51-64 (2014).

54 Li, B., Roberts, R. G. & Jacobs, Z. On the dose dependency of the bleachable and non-bleachable components of IRSL from K-feldspar: improved procedures for luminescence dating of Quaternary sediments. *Quaternary Geochronology* **17**, 1-13 (2013).

55 Galbraith, R. F., Roberts, R. G., Laslett, G. M., Yoshida, H. & Olley, J. M. Optical dating of single and multiple grains of quartz from jinmium rock shelter, northern australia: part i, experimental design and statistical models. *Archaeometry* **41**, 339-364 (1999).

56 Auclair, M., Lamothe, M. & Huot, S. Measurement of anomalous fading for feldspar IRSL using SAR. *Radiation measurements* **37**, 487-492 (2003).

57 Galbraith, R. Graphical display of estimates having differing standard errors. *Technometrics* **30**, 271-281 (1988).

58 Galbraith, R. & Roberts, R. G. Statistical aspects of equivalent dose and error calculation and display in OSL dating: an overview and some recommendations. *Quaternary Geochronology* **11**, 1-27 (2012).

59 Kirschvink, J. L. The least-squares line and plane and the analysis of paleomagnetic data. *Geophysical Journal of the Royal Astronomical Society* **62**, 699-718 (1980).

60 Lurcock, P. C. & Wilson, G. S. PuffinPlot : A versatile, user-friendly program for paleomagnetic analysis. *Geochemistry, Geophysics, Geosystems* **13**, 1-6, doi:doi:10.1029/2012GC004098 (2012).

61 Torsvik, T., Briden, J. & Smethurst, M. Super-IAPD Interactive analysis of palaeomagnetic data. *World Wide Web Address: http://www.geodynamics. no/software.htm* (2000).

62 Butler, R. F. *Paleomagnetism: Magnetic Domains to Geologic Terranes*. (Blackwell Scientific Publications, 1992).

63 Wilson, M. E. J., Bosence, D. W. J. & Limbong, A. Tertiary syntectonic carbonate platform development in Indonesia. *Sedimentology* **47**, 395-419 (2000).

Supplementary Table 1. Uranium-series ages of fossil tooth and bone samples based on sequential laser spot U-Th analyses.

Sample No	Lab. No.	Locality / depth below datum	element	DAD-Fitting 2-σ age range (kyr)
TLP10-1a	2947	Talepu T4; 3.4 m	*Celebochoerus* lower canine	161±15
TLP10-1b	2948	Talepu T4; 3.4 m	*Celebochoerus* lower canine	>255
TLP10-2	2942	Talepu T4; sieve, 3.3 m	*Celebochoerus* p^4	>600
TLP10-3	2956	Talepu T4; sieve, 3.4-3.6 m	*Celebochoerus* M^3 sin	214±24
TLP10-4	2954	Talepu T4; sieve, 3.4-3.6 m	*Celebochoerus* M^3 dex	>361
TLP10-6	2949	Talepu T4; sieve	bone fragment	230±38
TLP10-7	2951	Talepu T4; 3.6 m	*Celebochoerus* rib fragment	>353
TLP10-8	2946	Talepu T4; sieve	*Celebochoerus* I^1 sin	>248
TLP10-9	2955	Talepu T4; sieve, 3.4-3.6 m	*Celebochoerus* molar fragment	182±11

Supplementary Table 2. Sample burial depths, dosimetry data, equivalent dose (D_e) values and age estimates for the Talepu samples.

Sample code	Depth [a] (m)	Grain diameter (µm)	Water content [b] (%)	Gamma dose rate (Gy/ka)	External beta dose rate (Gy/ka)	Cosmic ray dose rate (Gy/ka)	Internal dose rate [c] (Gy/ka)	Total dose rate (Gy/ka)	D_e [d] (Gy)	Age [e] (ka)
					Upper Trench					
TUT-OSL1	287	180–212	20 ± 5 (19.8)	1.56 ± 0.02	2.51 ± 0.17	0.14 ± 0.01	0.84 ± 0.07	5.05 ± 0.19	518 ± 42 (8)	103 ± 9
TUT-OSL2	424	180–212	20 ± 5 (20.9)	1.60 ± 0.01	1.97 ± 0.13	0.12 ± 0.01	0.84 ± 0.07	4.53 ± 0.15	571 ± 45 (10)	126 ± 11
TUT-OSL3	440	180–212	20 ± 5 (13.9)	1.30 ± 0.01	2.45 ± 0.17	0.11 ± 0.01	0.84 ± 0.07	4.70 ± 0.19	664 ± 48 (12)	141 ± 12
TUT-OSL9	1007	90–180	20 ± 5 (10.6)	1.30 ± 0.01	2.75 ± 0.18	0.08 ± 0.01	0.60 ± 0.05	4.73 ± 0.19	740 ± 84 (13)	156 ± 19
					Lower Trench					
TLT-OSL6	800	180–212	30 ± 5 (29.8)	1.49 ± 0.01	1.85 ± 0.12	0.03 ± 0.01	0.84 ± 0.07	4.21 ± 0.14	>800 (8)	>190

[a] Below local ground surface.

[b] Values used for dose rate and age calculations, with measured (field) water contents shown in parentheses.

[c] Assuming K and Rb concentrations of 13 ± 1% and 400 ± 100 ppm, respectively.

[d] Weighted mean ± standard error, calculated using the Central Age Model and estimated from the individual single-aliquot D_e values for the sensitivity-corrected MET-pIRIR 250 °C signal. The number of aliquots is shown in parentheses. For the TUT samples, residual doses of 16–20 Gy (obtained from bleached aliquots of each sample) have been subtracted. The minimum D_e listed for TLT-OSL6 corresponds to the saturation dose of the MET-pIRIR 250 °C signal in 4 of the 8 aliquots (see text for discussion).

[e] Total uncertainty (1σ) includes the propagated random errors and a 2% systematic error to allow for any possible bias associated with calibration of the laboratory beta source.

Supplementary Table 3. Results from high-resolution gamma spectrometry for samples TUT-OSL2 and TUT-OSL3, and the corresponding beta dose rates and ages.

Sample	^{238}U (Bq/kg)	^{226}Ra	^{210}Pb	^{228}Ra	^{228}Th	^{40}K	Beta from K (Gy/ka)	Beta from U (Gy/ka)	Beta from Th (Gy/ka)	Ext. beta dose rate (Gy/ka)	Age (ka)
TUT-OSL2	41 ± 3	22.5 ± 0.6	25 ± 3	48.5 ± 1.6	47.6 ± 1.2	917 ± 24	1.72 ± 0.04	0.26 ± 0.02 [a]	0.23 ± 0.01	2.19 ± 0.10 [a]	124 ± 6 [a]
								0.32 ± 0.02 [b]		2.26 ± 0.10 [b]	122 ± 6 [b]
TUT-OSL3	37 ± 4	164.8 ± 1.8	120 ± 5	57.8 ± 2.1	65.4 ± 1.6	901 ± 26	1.69 ± 0.05	0.68 ± 0.04 [a]	0.27 ± 0.01	2.65 ± 0.12 [a]	136 ± 11 [a]
								0.29 ± 0.03 [c]		2.26 ± 0.10 [c]	147 ± 12 [c]

[a] These values were estimated based on the present (or measured) radioactivity of ^{238}U, ^{226}Ra and ^{210}Pb.

[b] These values were estimated based on the assumption that ^{226}Ra was depleted very recently and the decay chain of ^{238}U was in a long-term equilibrium (i.e., the radioactivity of ^{238}U, ^{226}Ra and ^{210}Pb were all equal to 41 ± 3 Bq/kg in the past). This assumption should yield a maximum estimate for the beta dose rate.

[c] These values were estimated based on the assumption that ^{226}Ra was excessed very recently and the decay chain of ^{238}U was in a long-term equilibrium (i.e., the radioactivity of ^{238}U, ^{226}Ra and ^{210}Pb were all equal to 37 ± 4 Bq/kg in the past). This assumption should yield a minimum estimate for the beta dose rate.

Supplementary Table 4. The single-aliquot regenerative-dose (SAR) protocol for multi-elevated-temperatures post-IR IRSL.

Step	Treatment	Observed
1	Give regenerative dose, D_i [a]	
2	Preheat at 320°C for 60 s	
3	IRSL measurement at 50°C for 100 s	$L_{x(50)}$
4	IRSL measurement at 100°C for 100 s	$L_{x(100)}$
5	IRSL measurement at 150°C for 100 s	$L_{x(150)}$
6	IRSL measurement at 200°C for 100 s	$L_{x(200)}$
7	IRSL measurement at 250°C for 100 s	$L_{x(250)}$
8	Give test dose, D_t	
9	Preheat at 320°C for 60 s	
10	IRSL measurement at 50°C for 100 s	$T_{x(50)}$
11	IRSL measurement at 100°C for 100 s	$T_{x(100)}$
12	IRSL measurement at 150°C for 100 s	$T_{x(150)}$
13	IRSL measurement at 200°C for 100 s	$T_{x(200)}$
14	IRSL measurement at 250°C for 100 s	$T_{x(250)}$
15	Solar simulator bleaching, 2 hr	
16	Return to step 1	

[a] For the 'natural' sample, i= 0 and $D_0 = 0$. The whole sequence is repeated for several regenerative doses including a zero dose and a repeated dose.

Supplementary Table 5. Sample burial depths, mean magnetic directions, and statistical parameters for sampled levels from the T2 and T4 excavations.

	Before demagnetization						After demagnetization				
Excavation-Depth[a] (cm)	Mean Declination	Mean Inclination	Number of samples	R[b]	*k*[c]	α 95[d]	Mean Declination	Mean Inclination	R	*k*	α95
T2-320	40.18	-18	4	3.99	591.68	3.8	25.7	-28.6	3.97	109.94	8.8
T2-510	31.7	-9.7	4	3.95	65.09	11.5	10.4	-9.8	3.95	54.76	12.5
T2-650	323.6	-67.9	4	3.96	73.97	10.8	320	-65.2	3.94	50.27	13.1
T2-750	320.3	-56.8	4	3.98	140.45	7.8	321	-53.9	3.95	62.65	11.7
T2-830	352	-10.3	4	3.86	21.75	20.2	359.4	-18.7	3.97	87.87	9.9
T4-180	332.7	-8.5	3	2.99	161.84	9.7	358.9	-7.7	2.99	166.96	9.6
T4-210	336.8	-15.9	4	3.98	178.52	6.9	359.9	-16.2	3.97	90.15	9.7
T4-240	337.5	-5.7	4	4.00	990.15	2.9	357.6	-3.4	3.99	403.9	4.6
T4-270	349	-2.5	3	2.98	122.56	11.2	4.6	-6	2.97	65.17	15.4
T4-320	345.2	-22.5	3	2.98	83.46	13.6	357.5	-19.7	2.97	73.8	14.5
T4-360	351.1	-1	4	3.95	57.25	12.2	0.8	4.8	3.99	223.81	6.2
T4-390	339.4	-9.2	4	3.98	150.67	7.5	348	-7	3.97	87.45	9.9
T4-420	346.2	2.9	4	3.97	99.09	9.3	355.5	4.2	3.98	139.56	7.8
T4-450	358.5	-23	3	2.95	41.24	19.4	4.6	-23	2.99	137.27	10.6
T4-480	357.5	-9.6	3	2.97	67.98	15.1	2	-5.4	2.98	120.6	11.3
T4-510	355.4	-9.6	4	3.98	187.53	6.7	2.5	-5.5	3.99	512.19	4.1
T4-550	356.2	-7.1	4	3.95	58.27	12.1	2.2	-8.7	3.98	142.25	7.7

T4-610	344.9	2.9	3	2.96	47.48	18.1	5.2	3.9	2.99	240.25	8
T4-640	344.5	-1.6	3	2.98	80.05	13.9	1.4	-3.6	3.00	661.1	4.8
T4-670	345.2	-13.9	3	2.99	150.22	10.1	355.7	-14	2.99	275.65	7.4
T4-710	344.7	0.2	4	3.97	112.63	8.7	357.3	2.8	3.99	331.1	5.1
T4-740	9.1	-15.8	4	3.90	31.54	16.6	4.9	-15.3	3.99	208.84	6.4
T4-770	354.2	-5.7	3	2.98	87.94	13.2	357.7	-2.2	2.96	51.09	17.4
T4-800	359.6	-5.8	3	2.99	236.46	8	40.8	-18	3.99	591.68	3.8

[a] Depth below local ground surface

[b] R is the vector resultant of the N site-mean Virtual Geomagnetic Poles[62]

[c] *k* is the precision parameter[62]

[d] Confidence limit within two standard errors from the calculated mean[62]

EXTENDED DATAFIGURES

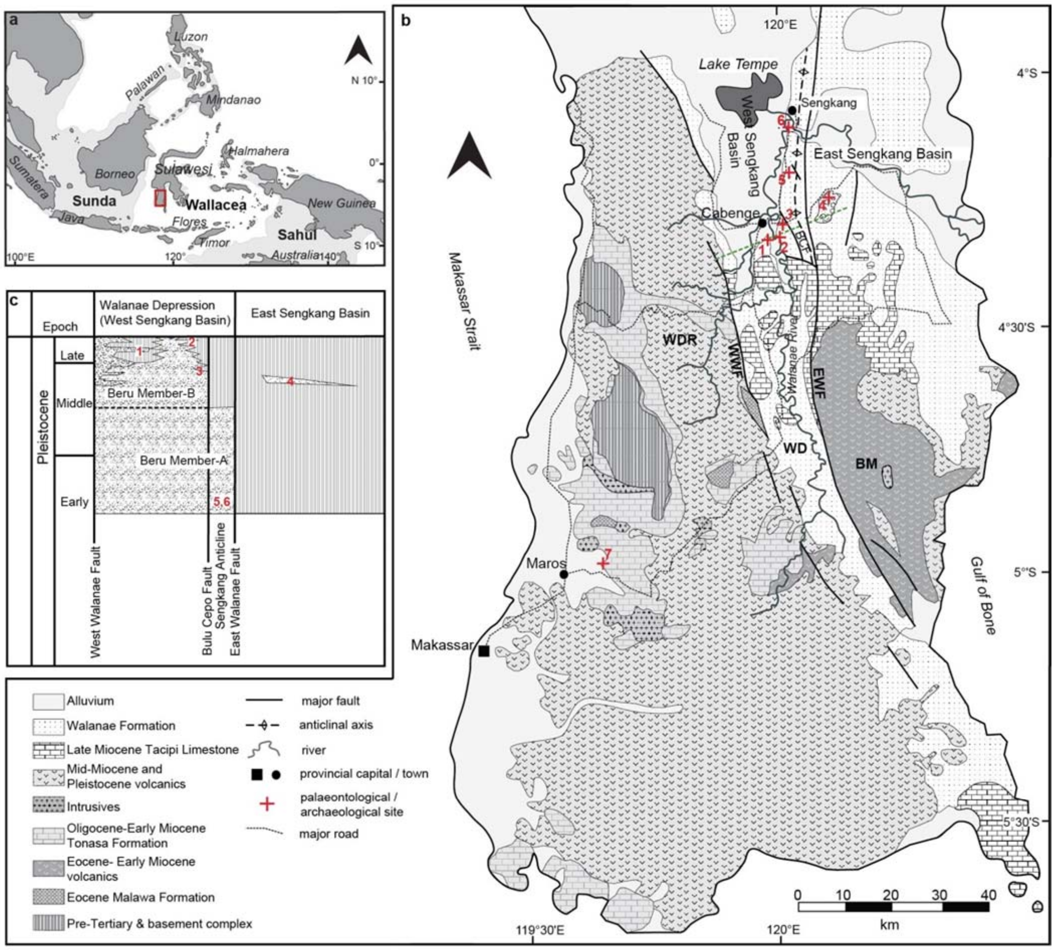

1

EXTENDED DATA FIGURE 1

Extended Data Figure 1. Geology of Southwest Sulawesi. **a**, Map of Southeast Asia showing the Sunda and Sahul continental shelves and the Wallacean island region in between. Area enclosed by red rectangle shown in **b**: Geological map of SW Sulawesi (modified after references[12,63]). The Walanae Depression (WD) is an elongate fault-bounded basin (also known as the West Sengkang Basin) separated from the Bone Mountains (BM) to the east by a major fault, the East Walanae Fault. To the west the basin is bordered by the Western Dividing Range (WDR) consisting of uplifted Miocene volcanic rocks deposited in a shallow marine environment[14]. The WD basin infill consists of a several km thick regressive sequence, named the Walanae Formation. In the southern part of the WD the Walanae Formation is folded and deformed by Pleistocene compression, whereas to the north near Lake Tempe deposition continues to the present day. 1: Talepu; 2: Paroto (alluvial terrace of the Walanae River); 3: Beru; 4: Tanrung River (Paleontological site: coastal terrace deposits); 5: Sompe; 6: Celeko; 7: Leang Bulu Bettue; **c**, Schematic stratigraphic scheme for the northern Sengkang Basin at the latitude of the Talepu site (green dotted line in b). The Walanae Formation basin fill represents a regressive sequence which was strongly influenced by tectonic movements along the Walanae Fault zone. The youngest unit of the Walanae Formation is the Beru Member (deltaic sands, clays and gravels), which contains fossil vertebrate remains of the Walanae Fauna[12]. The lower part of the Beru Member (A) is characterised by sedimentary structures indicative of shallow marine/estuarine/fluvial depositional environments. The upper part of the Beru Member (B) consists of fully terrestrial fluvio-lacustrine deposits, which merge into the modern floodplain along the depocentral axis of the WD. The coarser grained Unit B of the Beru Member was not deposited in the Sengkang Anticline, which started to rise during the Middle Pleistocene, nor in the southern portion of the WD South of Talepu. East of the Walanae Fault Zone, in the

East Sengkang Basin, uplift and folding during the Pliocene caused a depositional hiatus. Here Late Miocene deformed marine deposits of the Walanae Formation are unconformably overlaid by an up to 5 m thick fossil vertebrate-containing conglomerate, the Tanrung Formation, containing a distinct fossil fauna, the Tanrung Fauna[12]. During the Middle and Late Pleistocene, uplift of the Western Dividing Range generated the formation of alluvial fans and influxes of coarse-grained boulder conglomerates into the WD.

EXTENDED DATA FIGURE 2

Extended Data Figure 2. Talepu site images and excavations. **a:** View to the east of the N-S trending ridge. Talepu is located behind the palm trees on the left. **b:** Talepu excavation 2 in 2009. **c:** View towards the East Baulk of Talepu Excavation 2 in 2009. In 2010 the 1 x 2 m excavation was extended to a 2 x 2 m excavation. **d:** Talepu Excavation 4 in 2010. View towards the North Baulk. **e:** Talepu Excavation 2 in 2012. Photo shows the North Baulk at 4 to 5 m depth, with in the upper part the base of Gravel Unit A_7 and the three holes left by sampling for optical dating.

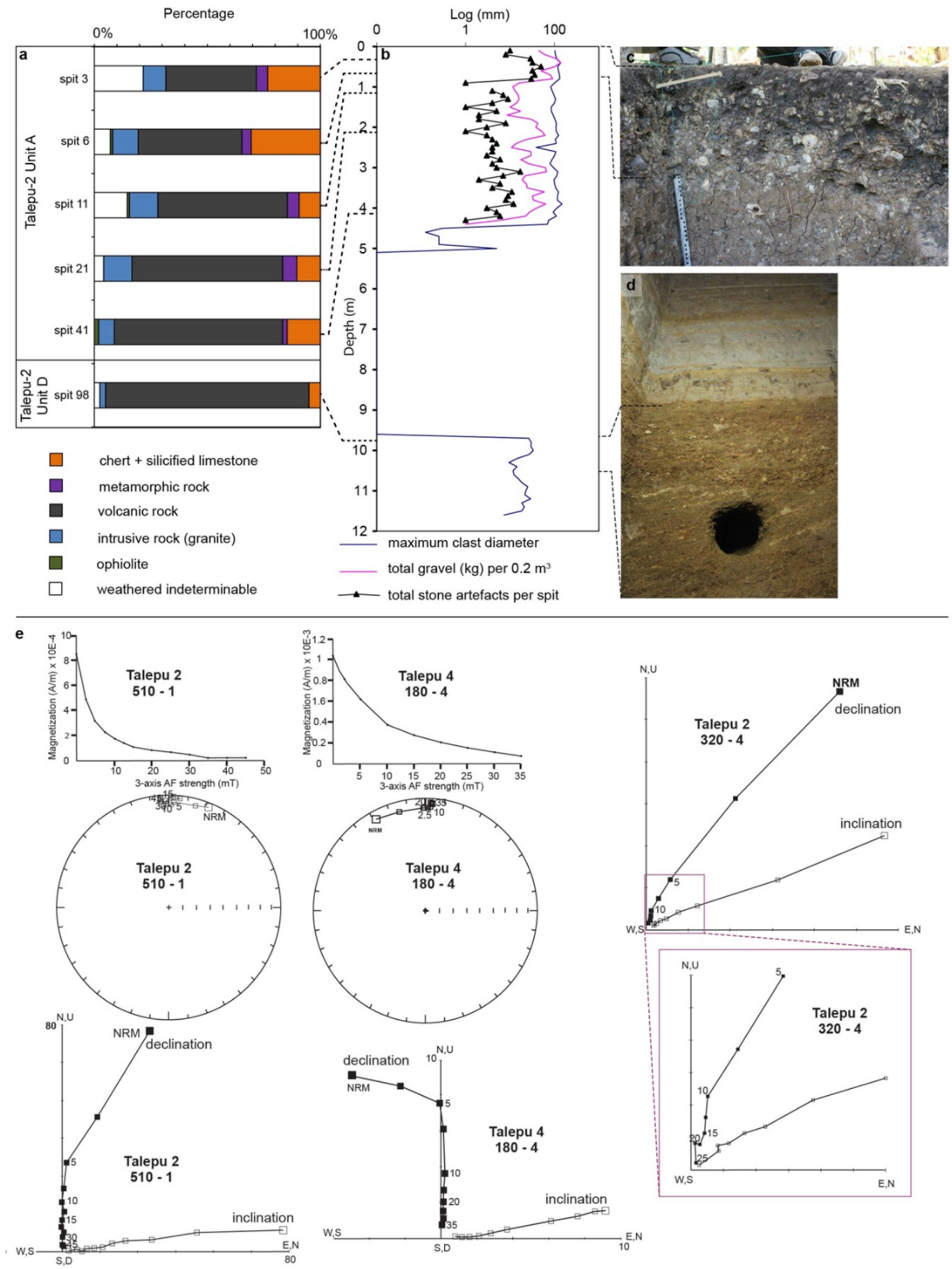

43

EXTENDED DATA FIGURE 3

Extended Data Figure 3. a, gravel compositions based on pebble counts (200 pebbles/level). Overall, the composition of the gravel is dominated by volcanic pebbles, which become more abundant with increasing depth, probably as a result of less intense weathering further down (near the surface the volcanic clasts are frequently weathered to a crumbly clayey "ghost"). Note the increase in both weathering-resistant silicified rock pebbles and heavily weathered indeterminable clasts towards the top of the sequence; **b**, Total number of artefacts per 10 cm spit (black triangles), total amount of gravel clasts per spit (red graph) and the maximum clast diameter per spit (blue graph: values represent the mean maximum clast diameter of the 10 largest clasts). Note the higher concentration of both gravel and artefacts in the topsoil: pebbles and artefacts are concentrated by winnowing of sand and clay by sheet-wash processes; **c**, Detail of the topsoil as exposed in the west baulk of Excavation T2; **d**, Detail of the basal sequence as exposed in the north baulk of Talepu excavation T2. Note the cross-bedded foresets of the pebbly sand of Layer D_2, with inter-bedded silt laminae, indicative of tidal activity. Diameter of the round sample hole (for optical dating) is ~ 10 cm; **e**, Representative NRM intensity plot of progressive demagnetization (upper left), equal area projections (middle left) and vector end-point demagnetization orthogonal plots (bottom left) for two Talepu palaeomagnetic samples (T2-510-1, T4-180-4). To the right the demagnetization curve for an additional sample (T2-320-4) is given. The inset shows the zoomed out trajectory endpoints of sample T2-320-4. Open squares on the equal area projection diagrams indicate an upper hemisphere magnetic direction.

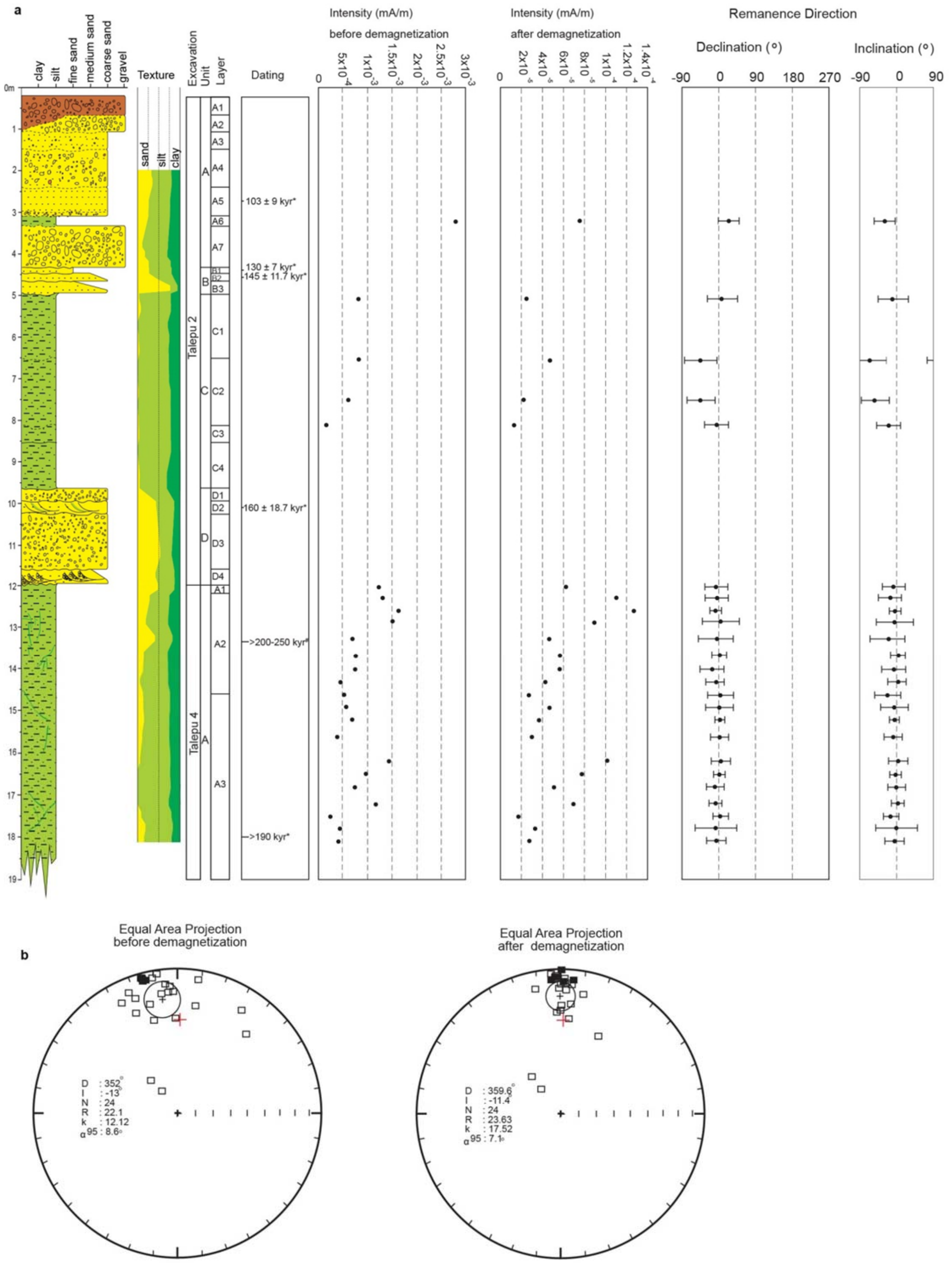

EXTENDED DATA FIGURE 4

Extended Data Figure 4. Lithological and magnetic properties against depth for the composite stratigraphic column at Talepu. **a**, Columns from left to right show lithology, sand/silt/clay ratios, Natural Remanent Magnetization (NRM) magnetic intensities before and after demagnetisation, magnetic declination and inclination directions. The intensities before and after demagnetisation represent averages for each sampled level. Declination and inclination values are the averages of the higher coercivity stable magnetization (ChRM); **b**, Equal area projections of NRM and ChRM directions for all sampled levels, and the mean direction (circles with crosses; the mean is of all sampled levels except the two levels with deviating inclinations: N = 22) and present-day magnetic direction in the area (red crosses).

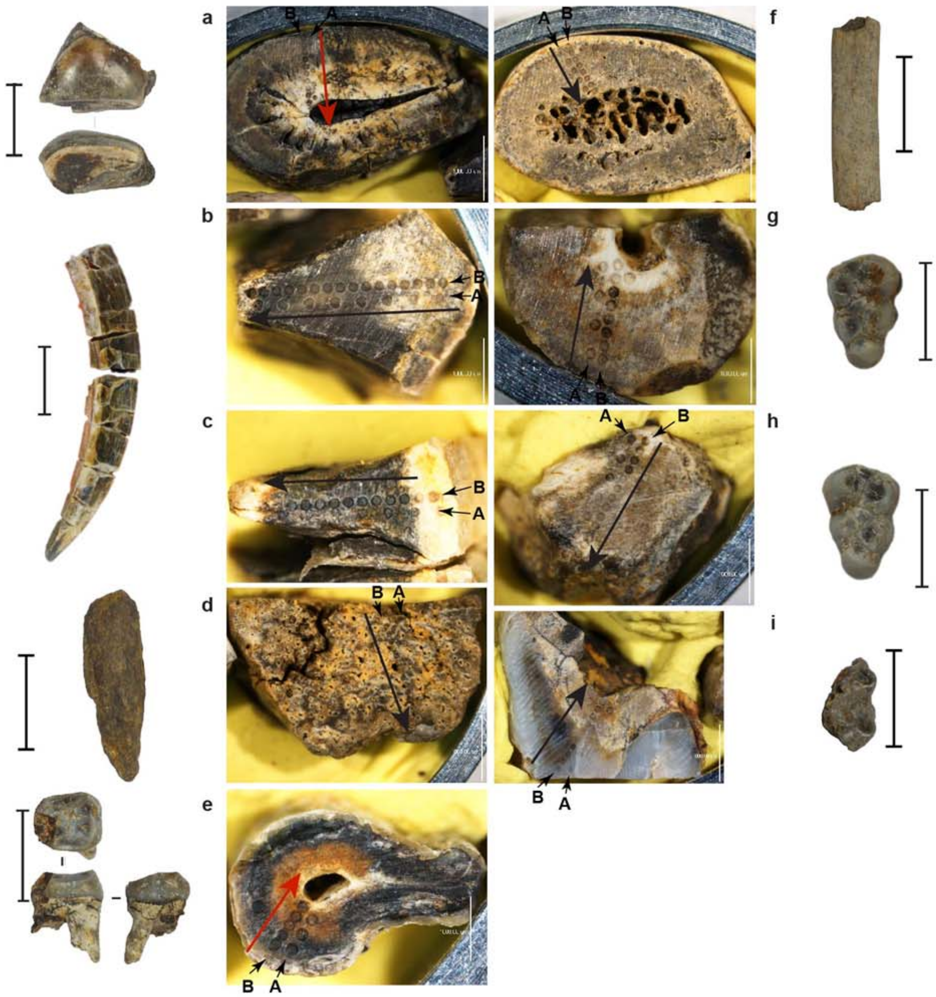

EXTENDED DATA FIGURE 5

Extended Data Figure 5. Faunal remains from Talepu excavation 4, used for U-series laser ablation dating (outer panels), and close-ups of the surface sections for each fossil with the laser spot profiles (central panels). All fossils originate from Excavation 4, Layer E_2. Numbers between brackets are Australian National University laboratory numbers. Scale bars next to fossils are 2 cm, white scale bars in close-ups are 1 mm. **a**, Specimen TLP10-F8 (ANU-2946), *Celebochoerus* left I^1; laser ablation transect on cut section of root; **b-c**, two sections measured on different transects of the same specimen, TLP10-F1 (ANU-2947 and ANU-2948), a *Celebochoerus* left lower canine; **d**, Specimen TLP10-F6 (ANU-2949), bone fragment; **e**, TLP10-F2 (ANU-2942), *Celebochoerus* upper left p^4; laser ablation transect on cut section of root; **f**, Specimen TLP10-F7 (ANU-2951), rib fragment of *Celebochoerus*; **g**, Specimen TLP10-F4 (ANU-2954), *Celebochoerus* upper left M^3; laser ablation transect on cut section of root; **h**, Specimen TLP10-F3 (ANU-2956), *Celebochoerus* upper right M^3 (same individual as previous); laser ablation transect on cut section of root; **i**, Specimen TLP10-F9 (ANU-2955), *Celebochoerus* upper molar fragment; laser ablation transect on cut section of enamel and dentine.

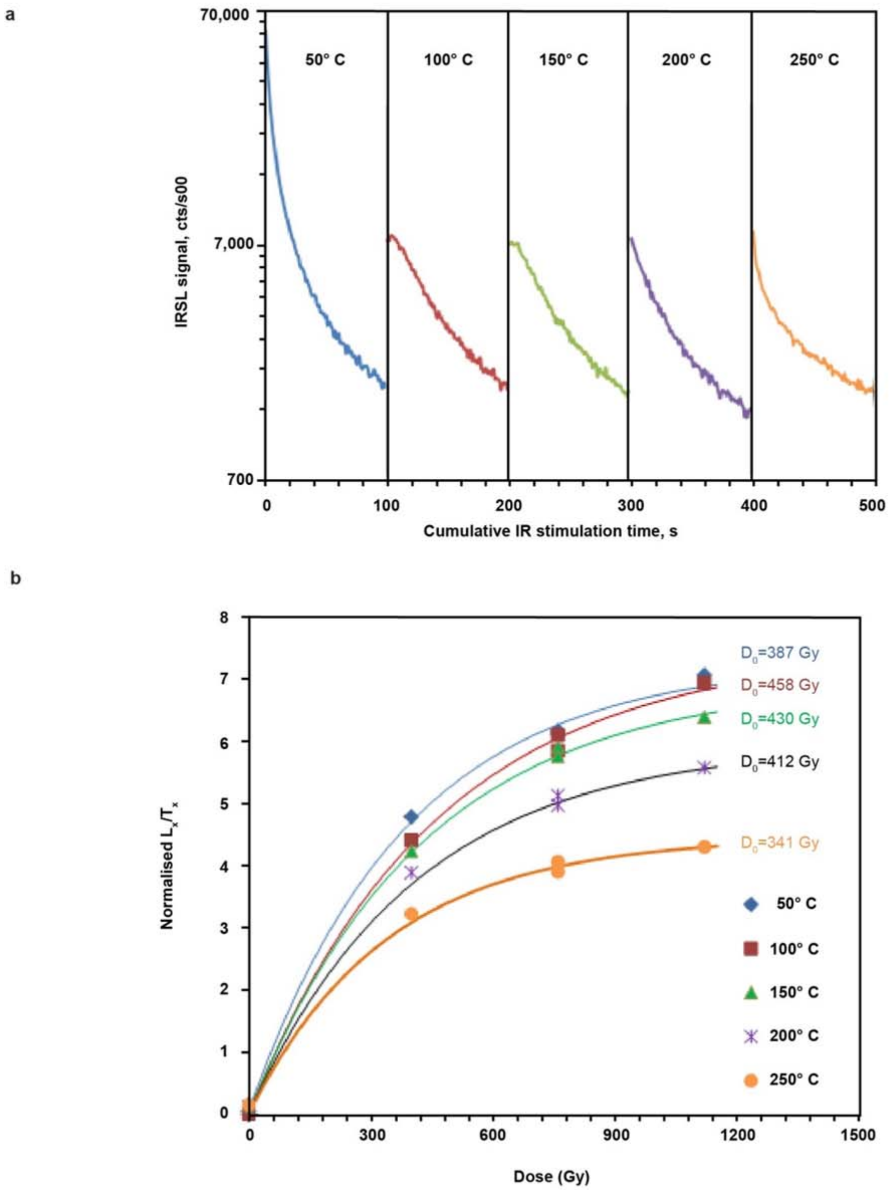

EXTENDED DATA FIGURE 6

Extended Data Figure 6. a, Representative IRSL and MET-pIRIR decay curves for a single aliquot of sample TUT-OSL2, stimulated at different temperatures (shown above each curve); **b**, Dose-response curves for the IRSL (50 °C) and MET-pIRIR (100–250 °C) signals for the same aliquot. The data points were fitted using a single saturating-exponential function. The best-fit curves are shown as solid lines and the characteristic saturation dose (D_0) values are also indicated.

a

b

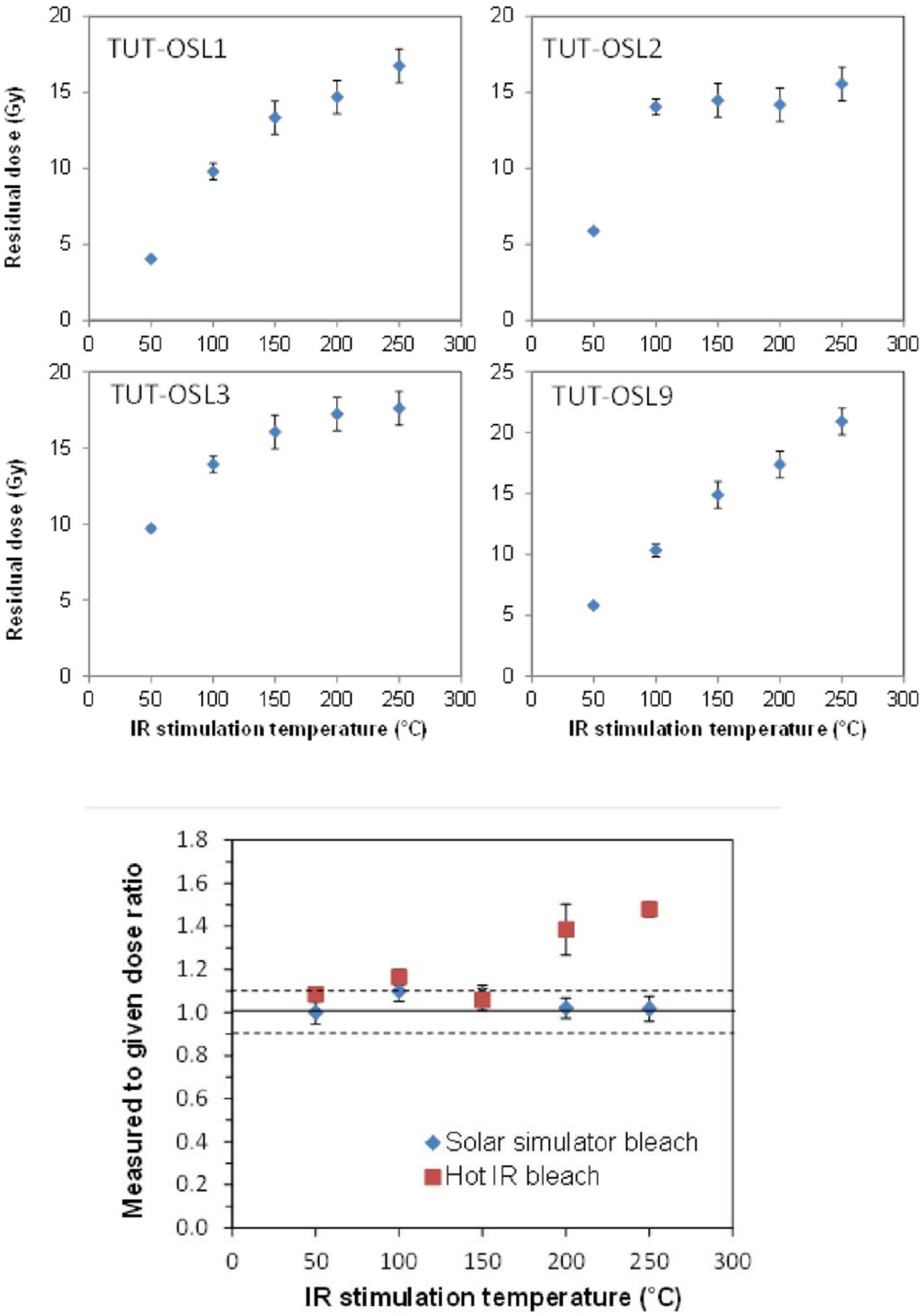

EXTENDED DATA FIGURE 7

Extended Data Figure 7. a, Residual doses measured for bleached aliquots of the TUT samples, plotted against stimulation temperature. Each data point represents the mean and standard error for 4 aliquots; **b**, Results of the dose recovery test conducted on sample TUT-OSL1. The measured/given dose ratios are shown for the IRSL and MET-pIRIR signals at the different stimulation temperatures. Each data point represents the mean and standard error for 4 aliquots. The data shown in red squares were obtained using a hot IR bleach at the end of each SAR cycle, as per the conventional MET-pIRIR procedure[41]. The data shown in blue diamonds were obtained with the modified MET-pIRIR procedure (**Supplementary Table 4**), using a solar simulator bleach instead of a hot IR bleach. The solid line denotes a ratio of unity, and the dashed lines indicate ratios 10% larger and smaller than unity. The data obtained using the modified MET-pIRIR procedure fall within the latter band.

a

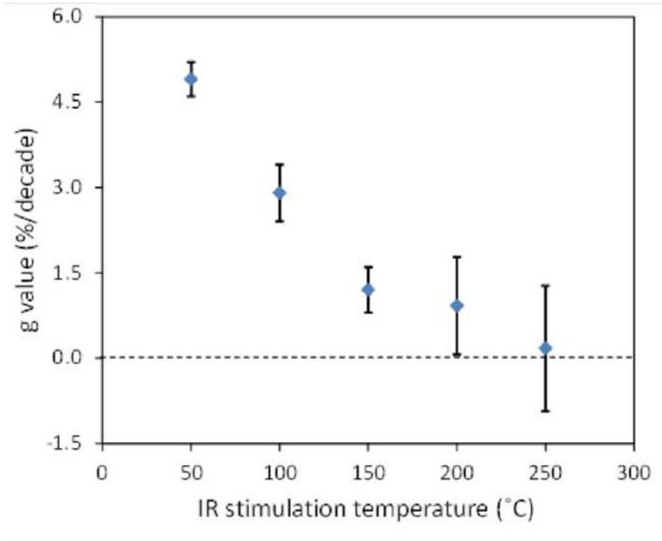

b

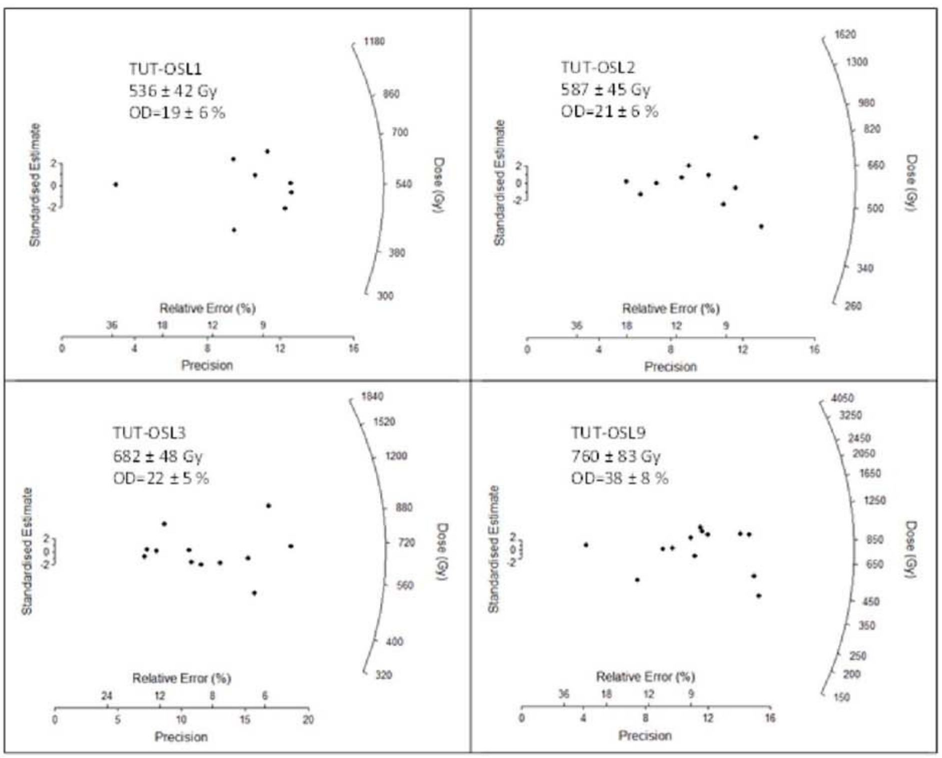

117 EXTENDED DATA FIGURE 8

Extended Data Figure 8. a, Anomalous fading rates (g-values) for the IRSL and MET-pIRIR signals of sample TUT-OSL3, plotted against stimulation temperature. Each data point represents the mean and standard error for 6 aliquots; **b**, Radial plots of single-aliquot D_e values for the TUT samples. Each plot also shows the weighted mean of the measured D_e values (i.e., before subtraction of the residual dose for each sample) and the overdispersion (OD) value for each D_e distribution, both estimated using the Central Age Model.

a

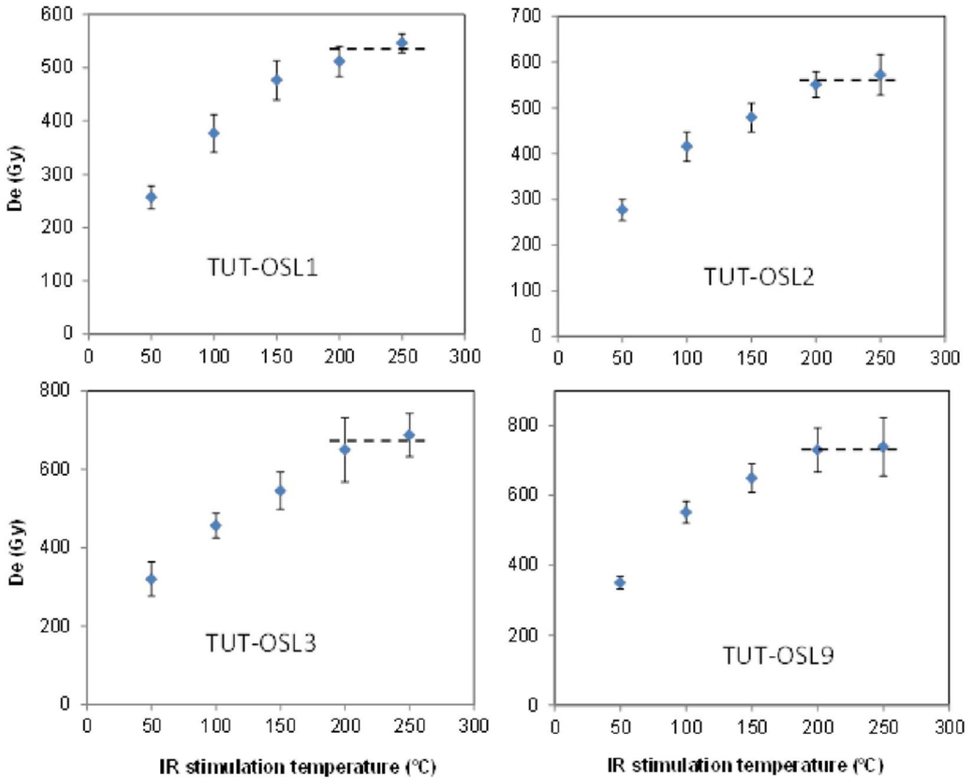

b

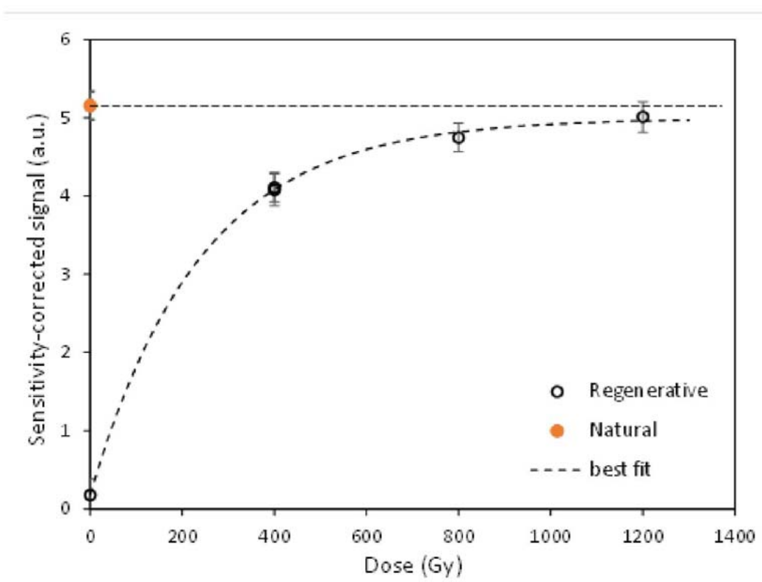

125 EXTENDED DATA FIGURE 9

Extended Data Figure 9. a, Plots of the weighted mean D_e against stimulation temperature for the TUT samples. The dashed line in each plot shows the plateau range of D_e values. Each data point represents the mean and standard error for 8 (TUT-OSL1), 10 (TUT-OSL2), 12 (TUT-OSL3) and 13 (TUT-OSL9) aliquots; **b**, Dose-response curve for the sensitivity-corrected MET-pIRIR 250 °C signal from an aliquot of sample TLT-OSL6. The regenerative-dose data points were fitted using a single saturating-exponential function, and the best-fit curve is shown as a dashed line. The natural signal of this aliquot (the orange circle on the y-axis) falls in the saturated region of the curve, so only a minimum D_e can be estimated.

a

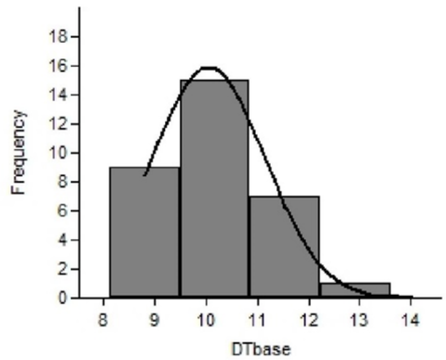

135

EXTENDED DATA FIGURE 10

Extended Data Figure 10. Histogram of the transverse diameter measurements of recent Lowland Anoa (*Bubalus [Anoa] depressicornis*) lower molars measured in the collections of NATURALIS, Leiden. The Lowland Anoa is the largest living Anoa, bigger in body size than the Mountain Anoa, *Bubalus [Anoa] quarlesi*. The lower molar fragment from Unit A of the Talepu-2 excavation (**Main Text Fig. 3t**) has a preserved transverse diameter of 14.4 mm and an estimated transverse width of 15.5 mm, slightly above the size range for recent Lowland Anoa.